Applied Surface Science 459 (2018) 788–801

Contents lists available at ScienceDirect

Applied Surface Science

journal homepage: www.elsevier.com/locate/apsusc

Full Length Article

# Controlled surface/interface structure and spin enabled superior properties and biocompatibility of cobalt ferrite nanoparticles

Sumayya M. Ansari[a], Bhavesh B. Sinha[b], Kalpana R. Pai[c], Suresh K. Bhat[d], Yuan-Ron Ma[e], Debasis Sen[f,g], Yesh D. Kolekar[a,*], C.V. Ramana[h,*]

[a] Department of Physics, Savitribai Phule Pune University, Pune 411007, Maharashtra, India
[b] Center for Nanoscience and Nanotechnology, University of Mumbai, Mumbai 400098, India
[c] Department of Zoology, Savitribai Phule Pune University, Pune 411007, Maharashtra, India
[d] Polymer Science and Engineering Division, National Chemical Laboratory, Pune 411008, India
[e] Department of Physics, National Dong Hwa University, Hualien 97401, Taiwan
[f] Solid State Physics Division, Bhabha Atomic Research Centre, Mumbai 400 085, India
[g] Homi Bhabha National Institute, Anushaktinagar, Mumbai 400094, India
[h] Department of Mechanical Engineering, University of Texas at El Paso, 500 W. Univ. Ave., El Paso, TX 79968, USA

ARTICLE INFO

*Keywords:*
Cobalt ferrite
Nanoparticles
Surface/interface structure
Surface spins
Superparamagnetism
Cytotoxicity

ABSTRACT

High quality, crystalline, well-dispersed, and stable magnetic oxide nanoparticles (NPs) of inverse spinel cobalt ferrite ($CoFe_2O_4$; CFO) were prepared by a facile, reproducible, and simple hydrothermal route. The transmission electron microscopy, small-angle scattering and X-ray diffraction analyses demonstrate the structural quality of CFO NPs with a controlled size of ~12 nm. Small-angle scattering experiments demonstrate that the pristine CFO NPs have the individual size ~8.5 nm and spherical shape. The Raman and infrared spectroscopic measurements further confirm their high chemical quality and cubic symmetry. CFO NPs exhibit a remarkable, maximum coercivity ($H_C$) value of 18.92 kOe, which is the highest value achieved to date. Surface spins and spins canting along with a weak dipolar interaction accounts for the giant $H_C$ and large effective anisotropy ($11.45 \times 10^6$ erg/cm$^3$) of these CFO NPs. The magnetic grain size of NPs reveals that the canted surface spins exist around the magnetic particles. Reorientation of surface spins and interparticle interaction causes the jumping behaviour in M-H hysteresis loops at H = 0. The cell viability of CFO NPs against the cancer (cisplatin resistant ovarian cancer – A2780/CP70) was evaluated to determine their potential application in biomedicine and health science. The mild response of CFO NPs in terms of their anti-proliferative nature against cancer cells and negligible cytotoxicity suggests their human-safe-and-friendly nature which makes them suitable for biomedical/health-related applications. Assessment of toxicity toward human red blood cells (RBC) revealed that hemolysis is less than 5% compared to the positive control confirming the potential applications of CFO NPs targeting human cells and making relevant for adopting them in biomedicine.

## 1. Introduction

Nanostructured and nano-particulate materials with controlled size, surface/interface chemistry and morphology while exhibiting enhanced or superior properties compared to their bulk counter parts are on demand for many of the current and emerging technologies [1–10]. Among the magnetic oxide nanoparticles (NPs), spinel ferrites have attracted a great deal of interest in view of their potential applications in various fields such as cell sorting, catalysis, ferrofluid applications, magnetic recording media, bio-sensors, magnetic resonance imaging (MRI), drug delivery, cellular signaling, hyperthermia, electronics, and biomedicine [2–20]. Among the family of these spinel ferrites, which can be represented by the chemical formula $MFe_2O_4$ (M = Mn, Co, Ni, Fe), cobalt ferrite ($CoFe_2O_4$; referred to CFO hereafter) is one of the most promising materials with a large cubic magnetocrystalline anisotropy (~1.8–3.0 × $10^6$ erg/cm$^3$ at 300 K) [8]. CFO exhibits unique characteristics such as higher Curie temperature (~793 K), moderate saturation magnetization (80 emu/g), higher coercivity (5400 Oe), excellent chemical-structural stability, large Kerr effect, Faraday rotation and good mechanical hardness at room temperature [9]. At the nanoscale dimensions, CFO often exhibits tunable, size-dependent physical and electronic properties [9,10].

* Corresponding authors.
*E-mail addresses:* ydkolekar@gmail.com (Y.D. Kolekar), rvchintalapalle@utep.edu (C.V. Ramana).

https://doi.org/10.1016/j.apsusc.2018.08.063
Received 22 November 2017; Received in revised form 25 July 2018; Accepted 6 August 2018
Available online 07 August 2018
0169-4332/ 

It is well known that the chemical and biological architecture of magnetic materials at the nanoscale dimensions has been currently introducing revolutionary trends in healthcare and medical therapies. Usually, the magnetic nanoparticles (MNPs) are smaller than 100 nm in comparison with the large bio-molecules such as antibodies, receptors and enzymes and being compatible with cells (10–100 μm), viruses (20–450 nm), proteins (5–50 nm) and genes (2 nm wide with 10–100 nm long) [11,12]. Furthermore, MNPs can undergo many interactions with biological molecules on the surface and inside the cells due to their size. Such MNPs are expected to significantly enhance the functional performance in cancer diagnosis and its treatment [11,12]. When surface/interface chemistry is controlled and biologically safe, MNPs are small enough to move inside the human body without affecting normal functions and can access the places which are inaccessible to other materials [12]. Note that the biological cells react with MNPs where the reactions can induce changes in cells, including cell growth or death [13]. Therefore, before using the MNPs for any application, specifically for biomedicine and health science related purposes, their functional cytotoxicity must be evaluated [14]. Also, several recent reports indicate that the MNPs significantly reduce the cell viability of human macrophage, human mesothelioma, and inhibit the formation of PC12 neuronal cell morphology [15,16]. The impetus for the present work is, therefore, to synthesize high-quality CFO NPs using a simple chemical approach and investigate the cytotoxicity effects of CFO NPs on the viability of human cells so that the cytotoxicity information required for biomedical and health science applications can be widened and readily accessible.

Several physical and chemical methods, such as hydrothermal, solvothermal, thermal decomposition, combustion, coprecipitation, precipitation, and electrospinning, hot injection method, were used to prepare CFO NPs and CFO-based composites [2,9,17–21]. However, an excellent control over the size, surface/interface chemistry, shape and distribution characteristics of CFO NPs are the key factors for their utilization in biomedical applications. It is well-known that the MNPs tend to agglomerate not only due to their large surface energy but also because of their strong magnetic interactions. Therefore, surface functionalization and/or synthesis modification has been integrated into many of the synthetic methods so as to obtain the desired properties of MNPs [22]. Moreover, using a capping agent or surfactant and polymer on MNPs to prevent the agglomeration is quite attractive specifically to derive a better functionality and to achieve better biocompatibility for health science related applications. In this context, in the present work, a chemical modification approach based on hydrothermal method is considered to design CFO NPs with superior structural and functional properties for biomedical applications. As demonstrated elsewhere, hydrothermal method for chemical modification is attractive to develop nanoscale materials for cancer treatment applications [2]. Here in this approach, we have modified the solvent by adding polyethylene glycol (PEG) as it is one of the polymers with a major interest in view of its non-toxicity, non-flammable nature and easy handling [21]. It has been demonstrated in the literature that PEG is very advantageous to prevent the agglomerations and hence to obtain reduced particle size while retaining structural order [21–24]. In fact, our results demonstrate the realization of high quality CFO NPs using this approach. The magnetic properties of nanoscale systems display unique size dependent magnetic properties that are sensitive to the synthesis method. Superparamagnetism, surface anisotropy and non-collinear (canted) spin structure are the most relevant effects associated with the size-reduction [24–31]. Also, size-reduction can influence the saturation magnetization ($M_S$) due to the fact that MNPs with smaller size may often have a high degree of spin-canting effects [32]. In addition, the magnetic interactions among the MNPs results into the large size agglomerates with different morphology. Therefore, for better understanding of the MNPs system, it is extremely important to understand the nature of agglomeration occurring at the surface/interface along with estimation of the accurate particle size. To address this issue and to provide fundamental insights, attempts were made to derive a deeper, fundamental understanding of the size and its distribution of CFO NPs. A strong attention has been paid in our work toward the fundamental understanding of the interplay between synthesis, surface/interface characteristics, controlled size and morphology, magnetic properties and cytotoxic effects. In this paper, we have demonstrated the synthesis of superior coercivity and bio-compatibility of CFO NPs via a simple one step, modified hydrothermal method at relatively lower temperature (180 °C). Magnetic properties of these CFO NPs are discussed comprehensively using the effects of surface spins and dipolar interaction. Finally, to address the successful integration of CFO NPs in nanomedicine and health science related applications, studies were made to explore the cytotoxicity studies of CFO NPs on viability of cancerous (A2780/CP70 Cisplatin resistant ovarian cancer) and non-cancerous (peripheral blood mononuclear cells) cells. We believe that the results, as presented and discussed thoroughly in this paper, will contribute not only to the current understanding and scientific advancement but also to further expand the cytotoxicity knowledge of magnetic NPs for future biomedical applications.

## 2. Experimental details

### 2.1. Materials and chemicals

Cobalt nitrate hexahydrate ($Co(NO_3)_2{\cdot}6H_2O$, 99.99%), iron nitrate nonahydrate ($Fe(NO_3)_2{\cdot}9H_2O$, 99.99%), potassium hydroxide (KOH) and polyethylene glycol solution (PEG-400) were obtained from Sigma Aldrich. All the chemicals were used as-received.

### 2.2. Synthesis of cobalt ferrite (CFO) nanoparticles

CFO NPs were synthesized using hydrothermal method in our previous work [2]; however, in the present study, synthesis protocol is modified with the addition of PEG solution as reported earlier [2]. Initially, the deionized (DI) water was used as a solvent and it is modified with the addition of PEG solution (30% of total experimental solution) and ultrasonicated for one hour. After that (1:2) molar amounts of $Co(NO_3)_2{\cdot}6H_2O$ and $Fe(NO_3)_3{\cdot}9H_2O$ were added and stirred until the reactants were dissolved completely. Then pH of the solution was adjusted to 12 by adding KOH solution (2 M) drop-by-drop so that the total solution volume becomes as 2/3 of the total volume of autoclave (250 ml). After the continuous stirring at 800 rpm for about 2 h, a homogeneous solution was obtained at room temperature. After that, the solution mixture was poured into a Teflon-lined autoclave, placed in an electric oven and heated at 180 °C for 24 h. After 24 h reaction, the Teflon lined bombs were allowed to cool down to room temperature naturally and prepared particles were separated from the liquid phase by centrifuge the final solution several times, at 10,000 rpm with DI water and absolute ethanol for 10 min. The liquid phase was discarded and the resulting black precipitates were dried in an oven at 100 °C overnight and finally, the pristine powder was used for further characterizations.

### 2.3. Physicochemical characterization and property measurements

#### 2.3.1. X-ray diffraction (XRD)

Crystallographic studies of CFO NPs were carried out using X-ray powder diffractometer (D8-Advanced Bruker). Cu $K_\alpha$ radiation ($\lambda$ = 1.5406 Å) with a 40 kV acceleration voltage and 40 mA tube current were used. The CFO sample was scanned slowly over a 2θ range of 20–80° at a scanning rate of 4 $min^{-1}$. As the Rietveld method is a well-established technique for extracting structural parameters and local bonding details from powder diffraction data, detailed structural evaluation of CFO NPS was performed using the Rietveld method. To generate the theoretical X-ray diffraction patterns, we have used the ICSD data having the collection code: 109044.

*2.3.2. Electron microscopy analyses*

Field-emission scanning electron microscopy (FE-SEM, JEOL-JSM-6360) and Transmission electron microscope (TEM, FEI Tecnai G2) were as used to analyse the surface morphology and particle size distribution. The size distribution of NPs was estimated with the image analysis of micrographs using *Image-J* software. EDS was used for the compositional analysis of pristine NPs. TEM images were obtained after placing a single drop (10 μL) of the aqueous solution of MNPs onto a copper grid coated with a carbon film. The grid was allowed to dry in air at room temperature for several hours. High-resolution images were acquired using an FEI Titan XFEG 60–300 kV spherical aberration-corrected microscope.

*2.3.3. Small-angle X-ray and neutron scattering experiments*

Small angle scattering experiments were performed to understand the mesoscopic structural information using the small angle X-ray scattering (SAXS) and small angle neutron scattering (SANS). The scattered intensities I ($q$) were recorded as a function of scattering vector transfer ($q = (4\pi\sin\theta)/\lambda$) where $\theta$ being the scattering angle and λ the X-ray wavelength (λ = 0.154 nm) and sample to detector distance was ~1070 mm. The higher $q$ regime (i.e. 0.1–2.3 $nm^{-1}$) has been investigated by performing SAXS using a laboratory based point collimation small angle scattering instrument. The intensities were corrected for sample absorption. Lower $q$ region (0.002–0.1 $nm^{-1}$) was probed by medium resolution SANS experiments. A double crystal based medium resolution SANS (MSANS) facility at the Guide Tube Laboratory of the Dhruva rector at Trombay, India was used for this purpose [33]. The instrument consists of a non-dispersive (1, −1) setting of (1 1 1) reflections from a pair of single crystals with specimen between them. The scattered intensities have been recorded as a function of wave vector transfer similar to SAXS. The incident neutron wavelength for the present experiment was 0.312 nm. The specimens under SANS investigations were placed on a sample holder with a circular slit of 1.5 cm diameter. The measured SANS profiles have been corrected for background and resolution effects [34]. SAXS and SANS data were normalized at the common $q$ region for the convenience of model fitting to such hierarchical structures. This would have been possible because the functionality of the scattering data at common $q$ region matches fairly well.

*2.3.4. Raman and infrared spectroscopy*

Raman spectra were recorded on an InVia Micro RAMAN (Renishaw) spectrophotometer with 532 nm laser excitation. Fourier transform infrared spectra (FTIR) were recorded using FTIR spectrometer (JASCO-6100) in the range of 400–4000 $cm^{-1}$.

*2.3.5. Dynamic light scattering and zeta potential measurements*

The stability of CFO NPs in DI water and Dulbecco's Modified Eagle's Medium (DMEM) was further determined by measuring zeta potential of the NPs using dynamic light scattering (DLS) (Brookhaven NanoBrook 90plus particles size analyzer). DLS was also used to measure the hydrodynamic diameter of CFO NPs in DI water and DMEM.

*2.3.6. Magnetic measurements*

Magnetic measurements were performed using the Quantum Design (QD) Evercool II PPMS 6000. The magnetization hysteresis i.e. M-H loops were measured at (300 K and 5 K) and at 385 K, by applying the magnetic fields up to 90 kOe and 5 kOe, respectively. The temperature dependence of magnetization, i.e. M (T), was measured under an applied magnetic field of 100 Oe and over a temperature range from 5 to 385 K. Zero-field-cooling (ZFC) and field-cooling (FC) procedures were performed.

*2.4. Cytotoxicity studies*

The cellular viability response to pristine CFO NPs was investigated using two types of cells, namely, Cisplatin resistant ovarian cancer cell line (A2780/CP70) and human PBMC (normal peripheral blood mononuclear cells) via a modified MTT assay. Details of cell culture, isolation of Peripheral Blood Mononuclear Cells (PBMC), and statistical analysis along with Cytotoxicity Assay of PBMC, Effect of Haemolysis Assay are mentioned in the supporting information.

Supplementary data associated with this article can be found, in the online version, at https://doi.org/10.1016/j.apsusc.2018.08.063.

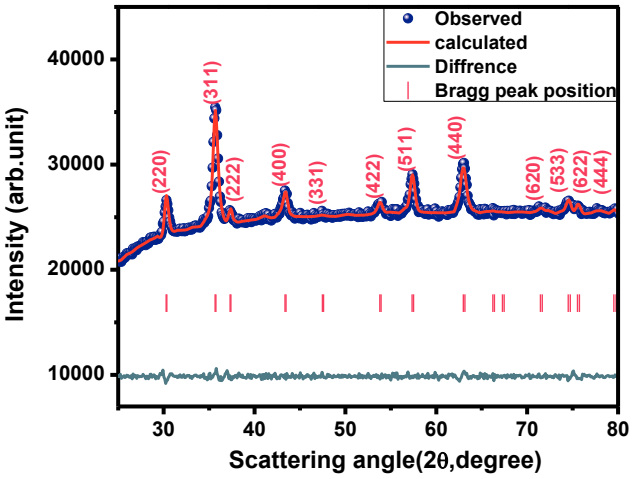


**Fig. 1.** XRD pattern of CFO NPs. The observed, calculated, difference patterns, and Bragg positions are shown.

## 3. Results and discussion

*3.1. Crystal structure of CFO NPs*

The phase of CFO NPs was confirmed by XRD patterns, which are shown in Fig. 1, where calculated and observed XRD patterns along with the differences are shown. Rietveld refinement was performed until the fitting yields a goodness factor, $\chi^2 \sim 1$. Rietveld refinement of XRD data confirms the single phase cubic spinel structure of CFO NPs without any impurities. The refinement parameters, the discrepancy factor ($R_{wp}$), expected values ($R_{exp}$), and $\chi^2$, are obtained as 17.7, 17.11, and 1.08, respectively, which are in good agreement with the reported parameters for ferrite systems [35]. The presence of intense diffraction peaks indicates the crystalline nature of CFO NPs. However, the peaks are rather broad which can be attributed to the smaller crystallite size. All the peaks were indexed according to the cubic spinel ferrite (JCPDS card no. 22-1086) structure with a space group Fd3m (2 2 7). The average crystallite size ($D$) was estimated based on integral width of the diffraction lines using the Scherrer's formula after background subtraction and correction for instrumental broadening [36] and for CFO NPs, the estimated value is $D \sim 12.29 \pm 0.15$ nm. However, the lattice constant is (8.343 ± 0.015 Å) is smaller than that of bulk CFO (8.391 Å). This may be due to the nano-size effects which include surface dipole interactions, surface tension and cation charge distribution within the nano-crystallite [37]. In general, the surface energy and surface tension of NPs are high leading to a reduction in the lattice parameter [2].The calculated X-ray density ($d_{x\text{-}ray}$) calculated is 5.367 $g/cm^3$.

*3.2. Morphology and chemical composition*

Fig. 2(a) represents the FE-SEM image of CFO NPs. Analysis of the SEM micrograph reveal that the presence of nano-size particles, which are spherical in shape with a uniform distribution. Note that the complexity of aqueous solutions i.e., changes in experimental conditions, can strongly influence the particle morphology [38]. However, the

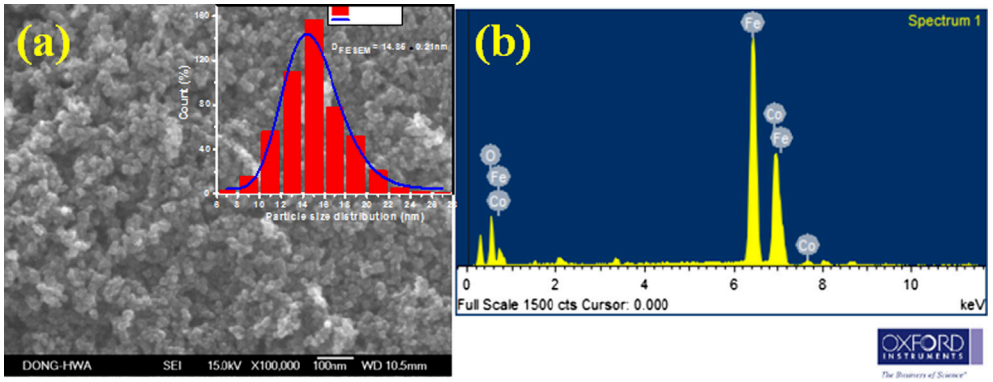


**Fig. 2.** (a) FESEM image of CFO nanoparticles along with inset shows the size histogram with log-normal-fitting curve (solid line) and (b) EDS spectrum of CFO NPs.

uniform, spherical morphology observed in this work is due to the PEG coating on CFO NPs. The PEG with uniform and ordered chain structure is easily absorbed at the surface of metal oxide colloid [39]. When the surface of a colloid adsorbs PEG, the colloidal activities decrease greatly and the growth rate will be confined to some facet [40]. Therefore, addition of PEG in the reaction system modifies the kinetics of growth process, which leads to anisotropic growth of NPs [37]. A statistical histogram of the particle size distribution (inset of Fig. 2(a)) illustrates that the diameter of CFO is in the range of 6–28 nm while the mean diameter is ~12 nm.

Furthermore, TEM image along with the corresponding histogram and the selected area electron diffraction (SAED) patterns of the CFO NPs are shown in Fig. 3(a–d). The SAED image (Fig. 3d) exhibits distinct pattern, which correspond to the diffraction from (2 2 0), (2 2 2), (4 0 0) and (4 4 0) crystal planes of CFO. Interestingly, careful examination of TEM image reveals that NPs exhibit both spherical and cubic morphology (Fig. 3a). For a better and deeper understanding, the statistical data of spherical and cubic shaped NPs are obtained separately and plotted the individual as well as combined histograms. For cubic morphology, the mean particle size is $D_{TEM\text{-}cube} \equiv 12.04 \pm 0.14$ nm with the polydispersity index, $\sigma \equiv 0.11 \pm 0.02$ (see Fig. S1(a)). The size determined from TEM is in agreement with the XRD result [$D_{XRD} \equiv 12.29 \pm 0.15$ nm]. Similarly, for spherical morphology, NPs are in the 6–15 nm range with an average particle size, $D_{TEM\text{-}sphere} = 10.12 \pm 0.38$ nm with $\sigma \equiv 0.16 \pm 0.06$ (Fig. S1(b)). Remarkably, we have observed the spherical and cubic morphology due to modified synthesis process. Thus, in order to evaluate the particle shape, an analysis of circularity distribution was carried out. The Circularity (C) is a parameter that represents how much the shape of a particle can be approximated. For an ideal spherical shape C is equal to 1, while it decreases as the particle shape deviating from sphere and changes to square and/or elongated. This parameter can be estimated from the area and perimeter of each particle [20]. In real particle systems, the spherical shape is associated with *C* values between 0.99 and 1, while the cubic morphology has *C* values around 0.8 [20]. In the present study, the observed circularities were found to be 0.999 and 0.786 for spherical and cubic morphology, respectively. It is noticeable that the circularities were observed to be uniform for all the spherical and cubic like shape particles. Furthermore, the CFO NPs prepared with 60% ($CFO_{P60}$) and 100% ($CFO_{P100}$) addition of PEG-400 solution are critically examined for the shape deviation from sphere to cubic and shown in Fig. 4(a–d), respectively. Notice that, with increase of PEG solution, the cubic morphology of particles becomes more foremost and simultaneously the presence of spherical particles turn out to be insignificant. Circularities for $CFO_{P60}$ and $CFO_{P100}$ are found to be approximately 0.781 and 0.784, respectively. It is well known that the size

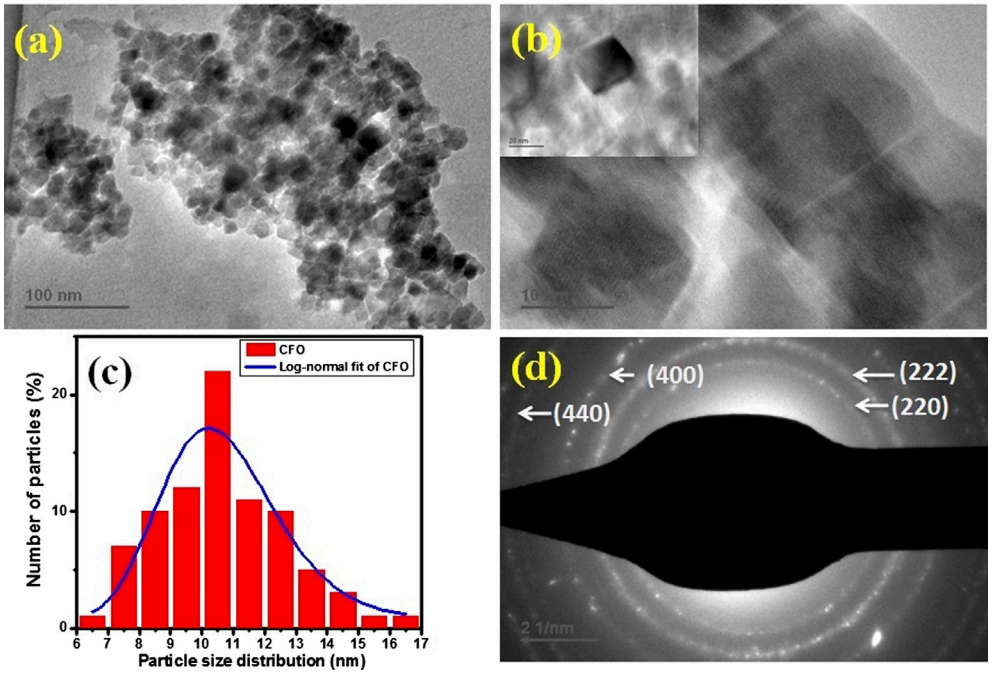


**Fig. 3.** TEM images of CFO nanoparticles (a and b) particle size distribution with Lognormal-fitting curve (solid line), (c) SAED and (d) obtained by TEM analysis.

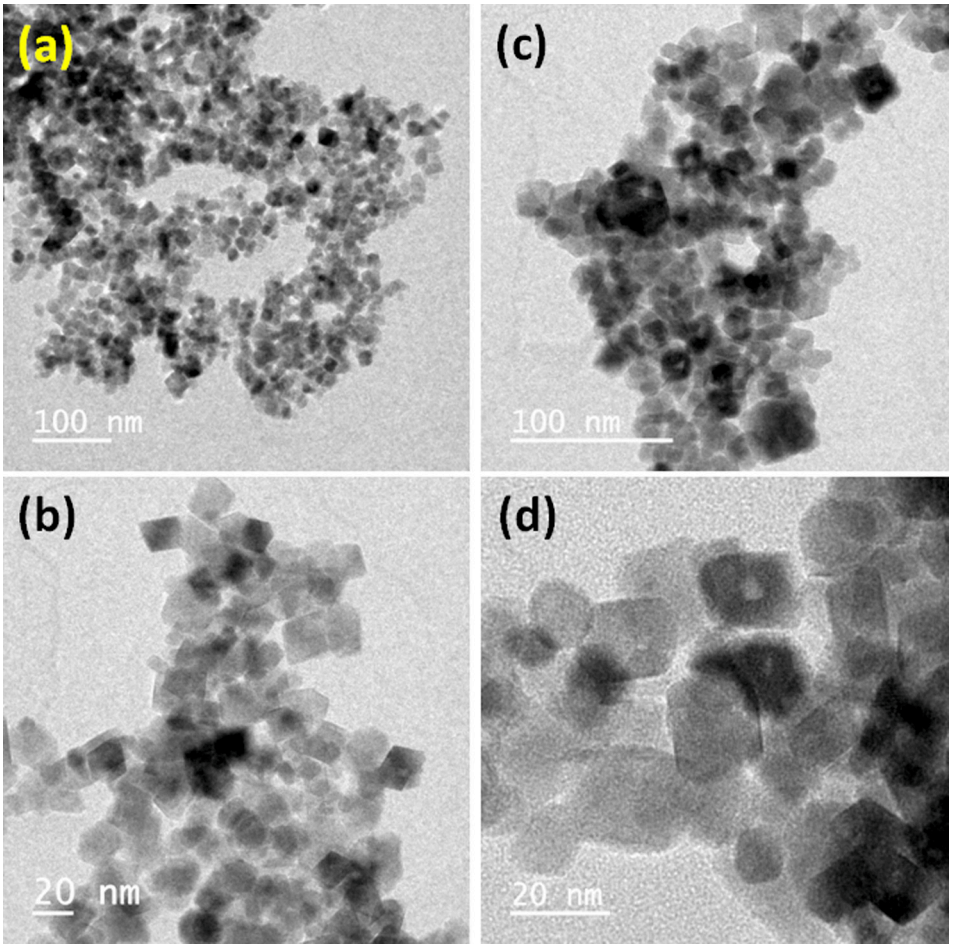


**Fig. 4.** TEM images of CFO nanoparticles ($CFO_{P60}$ and $CFO_{P100}$) prepared with 60% (a and b) and 100% (c and d) addition of PEG-400 in experimental solution, respectively.

**Table 1**
Summary of physical characteristics of CFO NPs determined from FESEM and TEM analyses.

| Median diameter of CFO NPs (nm) | Polydispersity index (σ) | Normalization constant (A) |
|---|---|---|
| $D_{FESEM}$ = 14.84 ± 0.20 | 0.17 ± 0.01 | 908.95 ± 65.55 |
| $D_{TEM\text{-}cube}$ = 12.04 ± 0.14 | 0.11 ± 0.01 | 12.48 ± 1.41 |
| $D_{TEM\text{-}sphere}$ = 10.12 ± 0.38 | 0.16 ± 0.06 | 59.21 ± 16.53 |
| $D_{TEM\text{-}cube\text{-}sphere}$ = 10.53 ± 0.28 | 0.17 ± 0.04 | 74.41 ± 12.07 |

and morphology are dependent on the competition between nucleation and growth kinetics that can be adjusted by controlling the reaction rate. As such, the size and shape of the NPs can be tuned by controlling the relative surfactant or capping agent concentrations. In the present study, PEG molecules were assumed to quickly attached to the lowest energy (1 0 0) facets and inhibit the growth of the NPs in (1 0 0) direction by forming a surfactant layer resulting in the formation of cubic shaped NPs. However, for lower PEG content (30%), the surfactant layer is not thick enough to reduce the growth in the particular direction and, thus, results in the formation of spherical shape NPs also observed. Thus, the modified hydrothermal method adopted results in both the spherical and cubic morphologies. Fig. 3(c) shows the combined histogram, where it is evident that the average particle size is $D_{TEM\text{-}sphere\text{-}cube}$ = 10.54 ± 0.28 nm with σ ≡ 0.17 ± 0.04. These results indicate that the CFO NPs have better dispersion and a narrower size distribution (polydispersity index < 20%) than those synthesized by a sol–gel auto-combustion method (20 ± 7 nm) and coprecipitation route (15–48 nm) [18]. The parameter obtained from FESEM and TEM micrographs are summarized in Table 1. Moreover, the EDS data of CFO NPs (Fig. 2b), represents that the samples exhibit desired stoichiometry (1:2) of Co: Fe which demonstrates that pristine CFO NPs are chemically homogeneous. Such chemical homogeneity coupled with narrow size-distribution is quite important for utilizing CFO NPs for medical and health sciences.

### 3.3. Local structure within the CFO NPs – Small-Angle Scattering (SAS)

The combined SANS and SAXS profiles of CFO NPs are shown in Fig. 5. The observed scattering contribution originates from the density fluctuations due to the presence of the NPs [41]. In the present case, two different length scales are associated with the system i.e., the size of (i) individual NPs and (ii) overall mass fractal like structures formed by the distribution of NPs. Thus, the total scattering signal consists of the additive contributions from both of these length scales. It is evident that the SAS profile within the overall accessible $q$ range (0.002–2.3 $nm^{-1}$) can be subdivided, for clarity, into two distinct regions, region I and region II (Fig. 5(a)). As the real space and the scattering space are connected by Fourier transform, region I ($q \sim$ 0.002–0.1 $nm^{-1}$) primarily contains the information about larger scale i.e., the overall size of CFO NPs in the distribution while region II ($q \sim$ 0.1–2.3 $nm^{-1}$) contains information on smaller density fluctuations, i.e., the size of individual CFO NPs. In our experimental setup, SANS cover the lower $q$ region whereas SAXS takes care of the higher $q$ scale. The NPs and their morphological distribution may be considered as the statistically self-similar i.e. fractals in nature; the scattering intensity is given by [42]:

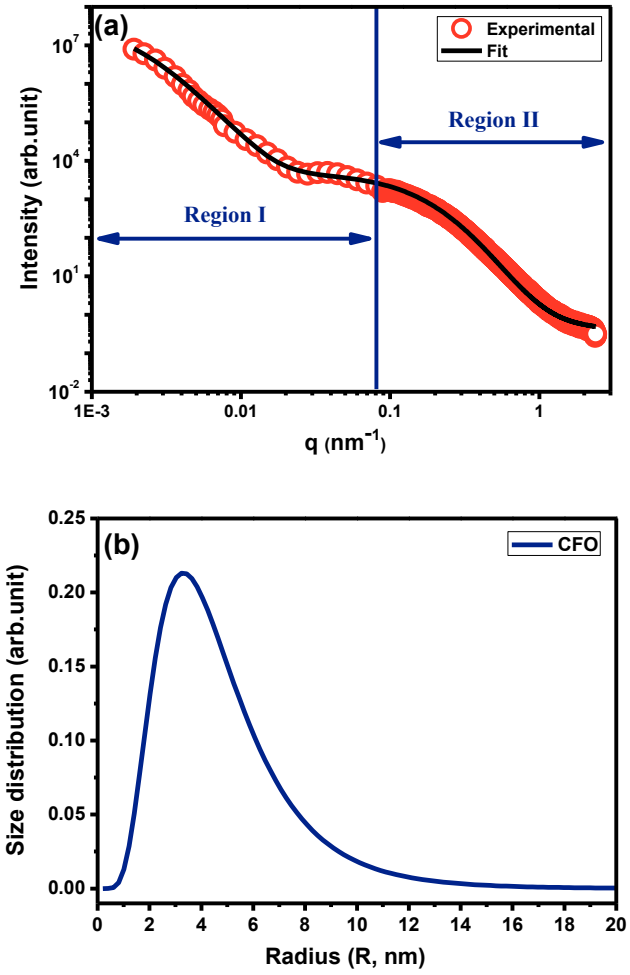


**Fig. 5.** SAXS and SANS profiles in double logarithmic scale (solid line represent the fitted curve) (a) and lognormal size distributions (b) of CFO NPs.

$$I_{frac}(q) = C_{frac} P_{frac}(q, r_0) S_{frac} s(q, r_0) \tag{1}$$

where $C_{frac}$ is scale factor which is independent of $q$ but depends on the number density of particles and the scattering contrast. $P_{frac}$ $(q, r_0)$ is a form factor of the basic units of the fractal with a radius $r_0$; and $S_{frac}(q, r_0)$ represents the structure factor for mass fractal [42]. A fractal like structure factor with the fractal dimension ($D_m$), monomer radius ($r_0$), cut-off function $h(r, \xi)$ with cut-off length $\xi$ of fractal correlation is expressed as:

$$S_{frac}(q, r_0) = 1 + \frac{D}{r_0^D} \int_0^\infty R^{(D-3)}.\, h(r, \xi).\, \frac{\sin(qr)}{qr}.\, r^2.\, dr \tag{2}$$

with Gaussian cut-off function is given by,

$$h_{Gauss}(r, \xi) = \exp\left[-\left(\frac{r}{\xi}\right)^2\right] \tag{3}$$

It is important to mention that there is another scattering contribution ($I_{np}(q)$) interacting polydisperse spherical particles model is assumed under a monodispersed approximation and can be expressed as [2]:

$$I_{np}(q) = C_{np} \int_0^\infty P_{np}(q, R) S_{np}(q, R) R^6 D_{np}(R) dR \tag{4}$$

where $C_{np}$ is the scale factor, $S_{np}(q, R)$ is the interparticle structure factor of the particle of radius $R$, which depends on the type of interaction and $P$ $(q, R)$ is the form factor of an individual NP of radius $R$ [43]. Thus, to analyze the present data, a spherical form factor [44] is considered as:

$$P_{np}(q, R) = 9\left[\frac{\sin(qR) - qR\cos(qR)}{(qR)^3}\right]^2 \tag{5}$$

$D_{np}(R)$ represents the size distribution of particles, i.e. D(R)·dR is proportional to the probability of finding a particle with radius R to R + dR. A standard normalized log-normal distribution was assumed in the following form:

$$D_{np}(R) = \frac{N}{\sqrt{2\pi\sigma^2} R} \exp[[\ln(R/R_o)]^2/2\sigma^2] \tag{6}$$

Here $\sigma$ as the polydispersity index, $R_0$ is the median radius of the particles and $N$ represent a normalization factor. Therefore, considering both the contributions the total scattering intensity can be written as:

$$I_{total}(q) = I_{frac}(q) + I_{np}(q) \tag{7}$$

$$I_{total}(q) = C_{frac} P_{frac}(q, r_0) S_{frac}(q, r_0) + C_{np} \int_0^\infty P_{np}(q, R) S_{np}(q, R) R^6 D_{np}(R) dR \tag{8}$$

Here, $I_{np}(q)$ is the scattering contribution from individual nanoparticles and $I_{frac}(q)$ is the scattering contribution from the NPs (as we have observed from the SEM micrographs, where CFO sample shows NPs well distributed on the surfaces). In order to fully understand size distribution of the system, the model scattering intensity has been fitted to the experimental SAS profiles using nonlinear least square method to obtain the unknown parameters, namely, size distribution, fractal dimension ($d_m$) and radius of gyration ($R_g$). The radius of gyration defines the average distance from the center of mass to each individual NP. The fractal dimension found to be ~2.7. The fit of equation with the data are shown in Fig. 5a. Similarly, Fig. 5b shows the size distribution obtained from combined SAS fit. It is evident that the model is indeed capable of explaining the scattering data in the complete $q$ range. Interestingly, it has been found that the mean radius, $R_o$ ~ 4.24 nm with $\sigma$ ~ 0.48. However, the median particle size ($2R_o$) obtained from the SAXS measurements is smaller than the size (12.27 nm) obtained from the XRD and TEM. A justification for the observed discrepancy is a result of the sensitivity and selectivity of the respective analytical tool [2]. Briefly, the size extracted from XRD is fully based on the crystalline domains and the smallest subunit particles present in the powders are treated amorphous or embedded in an amorphous matrix. On the other hand, SAXS is quite sensitive and can determine the size from both the amorphous and crystalline particles and the size extracted from SAXS thereby become smaller than the size extracted from XRD data.

### 3.4. Chemical bonding

#### 3.4.1. Infrared spectroscopy

The FTIR spectra of CFO NPs are shown in Fig. 6. In spinel ferrites, the IR absorption bands are produced due to the vibration of oxygen ions with the cation present at the octahedral and tetrahedral sites in the unit cell. It is seen that the IR spectrum of CFO NPs shows many characteristic absorption peaks at 3465, 2929, 2859, 1581, 1385, 1034, 959,602 and (412, 425, 438) cm$^{-1}$ – all of these are in agreement with the literature [45]. The absorption peak at 3465 cm$^{-1}$ is attributed to the stretching vibration of the hydroxyl groups indicating the presence of free and absorbed water on the surface of NPs. The peak at 959 cm$^{-1}$ is attributed to the O—H out of plane vibration. Moreover, the other two weak peaks at 2859 ($\nu_s$ C—H), and 2929 ($\nu_a$ C—H) cm$^{-1}$, respectively, arise from the symmetric and asymmetric stretching vibration of C—H bond (see Fig. 6b). A sharp band observed at 1581 cm$^{-1}$ corresponds to the stretching vibration of —C—$CH_2$ groups. These three bands observed at 1581, 2859 and 2929 cm$^{-1}$, known as the characteristic bands of $CH_2$ groups, indicate the successful ligand exchange. The IR spectra also

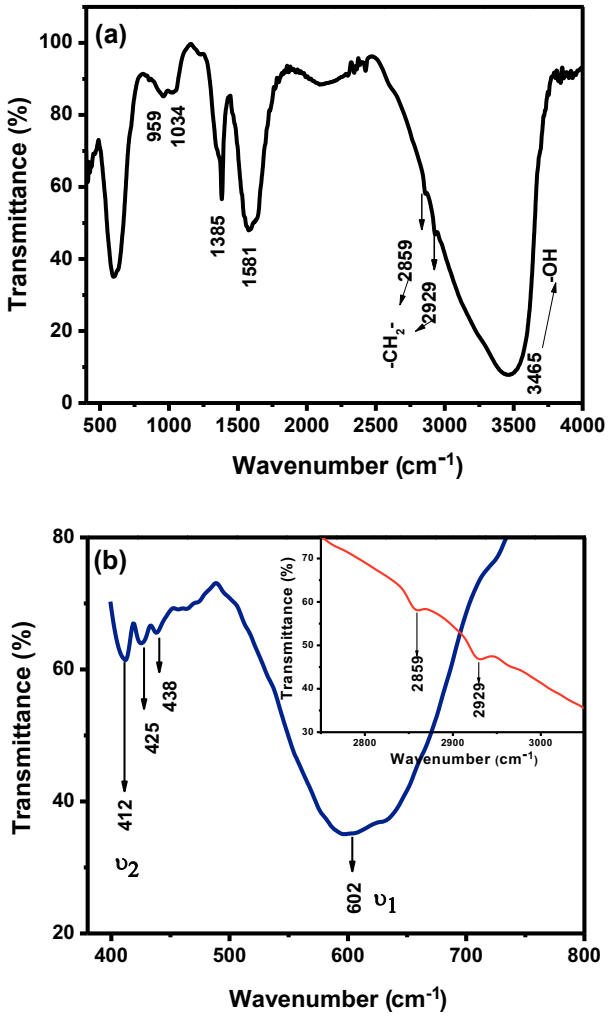


**Fig. 6.** FTIR spectra of CFO NPs (a) for 400–4000 $cm^{-1}$ along with magnified data for clarity and (b) from 400 to 800 $cm^{-1}$ (inset plot shows the symmetric and asymmetric stretching vibrations of C–H bond).

exhibit (Fig. 6(b)) the two absorption bands below 700 $cm^{-1}$ which is a common feature of spinal ferrite NPs [2]. The absorption bands observed at 602 $cm^{-1}$($\nu_1$) and ~412–438 $cm^{-1}$ ($\nu_2$) confirm the formation of single phase spinel structure having two sub-lattices, tetrahedral (A) site and octahedral (B) site [2]. The absorption band $\nu_1$ is caused by the stretching vibrations of the tetrahedral metal ($Fe^{3+}$)–oxygen bond while the absorption band $\nu_2$ is caused by the octahedral metal ($Co^{2+}$)–oxygen vibrations at octahedral sites. The presence of these two IR bands is the signature of phase purity of CFO NPs [2]. The difference in intensities of $\nu_1$ and $\nu_2$ may be attributed to the changes in bond lengths ($Fe^{+3}$–$O^{2-}$) within the octahedral site and tetrahedral site. In addition, the observed slight splitting of the octahedral absorption band near $\nu_2$ is correlated to the presence of different kinds of cations, including Co(II), Fe(III) and Fe(II) on the "B" site. This is attributed to the "Jahn–Tellar" distortion produced by Fe (II) ions that results into the local deformation in the crystal field potential, and thus thereby splitting the absorption band [46].

### 3.4.2. Raman spectroscopy

Raman spectra of experimental and fitted data of CFO NPs are presented in Fig. 7. The well-defined peaks observed in Raman spectra support the presence of high quality, cubic crystal lattice symmetry and can be used to better understand mechanism of molecular-vibrational modes present in CFO NPs. CFO has an inverse cubic spinel structure that belongs to the space group *Fd3m* ($O_h^7$). Group theory predicts five

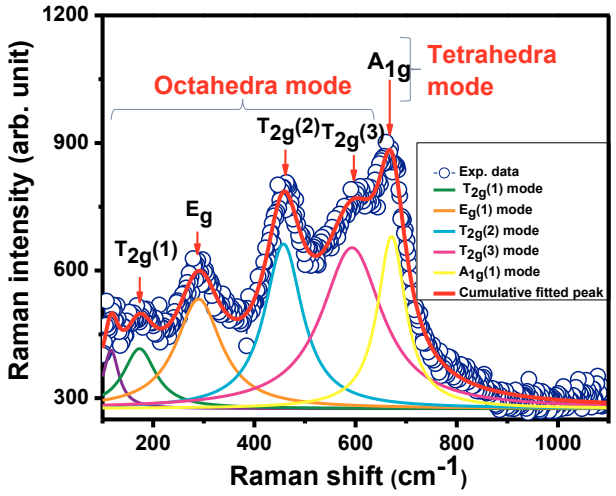


**Fig. 7.** Raman spectra of CFO NPs recorded at room temperature.

**Table 2**
Raman vibrational data along with the assigned mode for CFO NPs.

| Peak position ($cm^{-1}$) | FWHM ($cm^{-1}$) | Area ($cm^{-2}$) | Peak height ($cm^{-1}$) | Raman active mode | Assigned Polyhedra |
|---|---|---|---|---|---|
| 173 | 78 | 17,304 | 141 | $T_{2g}(1)$ | $FeO_6$ octahedra |
| 290 | 109 | 44,123 | 258 | $E_g$ | |
| 458 | 91 | 55,354 | 387 | $T_{2g}(2)$ | |
| 593 | 146 | 86,820 | 378 | $T_{2g}(3)$ | |
| 671 | 68 | 43,286 | 405 | $A_g$ | $FeO_4$ tetrahedra |

Raman active modes, i.e., $A_{1g}$ + $E_g$ + $3T_{2g}$ present in the cubic spinel [2]. Therefore, all the five Raman peaks are assigned to the vibrational mode of *Fd3m* space group and are tabulated in Table 2. Assignment of these phonon modes were carried out in accordance with the literature. The un-assigned weak shoulder peak observed at 117 $cm^{-1}$ is attributed to the defect, surface disorder or oxidation of metal cations. The peak at 671 $cm^{-1}$ is due to $A_{1g}$ symmetry involving symmetric stretching of oxygen ion with respect to metal ion in tetrahedral void. The other low frequency phonon modes i.e., $E_g$ and $3T_{2g}$, are due to the metal ion involved in octahedral void ($BO_6$). These modes correspond to the symmetric and asymmetric bending of oxygen ion in M–O bond at octahedral voids [2]. All the Raman modes observed for CFO NPs are symmetric in nature. This observation supports the fact that the CFO NPs exhibits the phase purity.

### 3.5. Dynamic light scattering and zeta potential measurements (colloidal stability)

The DLS measurements shed light on the effect of modified solvent on overall size (ferrite core + organic coating of PEG) and the size distribution of CFO NPs. A marked difference was noted when the pristine CFO NPs were dispersed in DI water and DMEM in terms of the hydrodynamic diameter ($R_H$) and corresponding dispersion state. It has been observed that the CFO NPs exhibit the smaller $R_H$ in water ($R_{H\text{-}water}$ ~ 212 nm) compared to DMEM ($R_{H\text{-}DMEM}$ ~ 314 nm) as a solvent. This could be due to the suppression of the double layer of ions around the particles. Thus, compared to DMEM, water suppresses the double layer of ions, enhancing the diffusion speed and resulting in smaller $R_H$ in water. In addition, a discrepancy in size measurements from other physical methods (TEM, Fe-SEM, SAS, and XRD) and DLS techniques is also noted. The size of CFO NPs obtained from DLS is higher; however, this observation is consistent with the previous findings [47]. Several

reasons were postulated to offer explanation for such differences [47–49]. In this work, the $R_H$ of CFO NPs and their surrounding solvent layers may the primary reason. The presence of PEG, as seen by infrared spectroscopy, also supports the fact that the PEG organic layer is encapsulating the CFO NPs. Bregar et. al. have reported that the NPs in suspension are composed of a few primary crystallites forming the agglomerate [48]. Since these agglomerates cannot be divided and behave as a single particle, individual agglomerates will be referred to as NPs (NP cores). Whereas Mazz et al. [49] and Bohara et al. [50] have independently reported that, even in the absence of external magnetic field, the magnetic dipole–dipole interactions between the particles can cause their agglomeration. Therefore, the hydrodynamic size distributions are larger than those observed by FESEM and TEM. Sinko et al. [51] have also found that the size derived from DLS is 2–3 times larger than the size obtained from SEM. Also, in the SAXS experiments, dried powders were used in vacuum while the particles are dispersed in a solvent in DLS. The NPs can be hydrated or solvated in polar solutions. The discrepancies in size might be attributed to the hydration/solvation shells. Tobler et al. provide further explanation for the size difference and suggested that the highly hydrous and open-structured particles can collapse because of the dehydration and relaxation processes under high vacuum [52].

For NPs, zeta potential is an extremely crucial parameter because it is a direct measure of the potential stability of a colloidal system. In present study, the stability of NPs in DI water and DMEM are evaluated. The Z-average i.e. $\xi$ values were calculated as the average of ten measurements of the same suspension. In the present study, zeta potential values are $-18.06$ mV and $-16.79$ mV in DI water and DMEM solvent, respectively. In general, the NPs with negative zeta potential are stable due to the electrostatic repulsion among the NPs. Zeta potentials of pristine CFO NPs in water show that all the particles are negative charged. The results are in excellent agreement with those reported by Shen et al. [53]. Note that the NPs suspension is generally considered to be stable if a zeta potential value exists in the $+30$ mV to $-30$ mV range [47]. Therefore, the dynamic light scattering measurements and zeta potential studies provide strong evidence for these CFO NPs are stable in as both as-is and dispersed in solvent media. Thus, the structure, size, morphology, chemical bonding and stability measurements suggest their applicability in health science applications.

### 3.6. Magnetic properties

The magnetization (M-H) loops at 5 K, 300 K and 385 K of CFO NPs are shown in Fig. 8 and the parameters obtained from (M-H) loops are listed in Table 3. It is seen that the observed value of $M_S$ at 5 K is $\sim 3.18\ \mu_B$/F.U., which matches well with the literature value [57]. Considering the formula $(Co_{1-\delta}Fe_{\delta})\ [Co_{\delta}Fe_{2-\delta}]\ O4$ to describe the cation distribution in the spinel structure of the CFO NPs and assuming that $Fe^{3+}$ and $Co^{2+}$ ions have magnetic moment of $5\ \mu_B$ and $3\ \mu_B$, respectively, the inversion parameter is obtained to be $\delta \sim 0.95$. This value of inversion parameter indicates that the crystal structure of CFO NPs is very close to the inverse spinel. Furthermore, at 300 K, it is observed that the $M_S$ value for CFO NPs (63.53 emu/g) is less than that of the bulk CFO (80 emu/g) for an applied field of $\pm$ 90 kOe. Reduction in $M_S$ is attributed to the surface disorder or spin canting at the NP surface [54]. At 5 K, the $M_S$ and $M_r$ value increases to 72.79 emu/g and 58.71 emu/g, respectively; this observation is consistent with the previous studies [55]. The observed increase/decrease in $M_S$ for larger/smaller particles is likely due to the particles internal spin structure, which consists of a spin-ordered core and spin-disordered shell due to either spin canting or surface anisotropy [56]. However, in these CFO NPs, we believe that the simultaneous effect of spin disorder or spin canting, effective anisotropy (surface anisotropy) and interaction among the NPs play a key role. It is important to note that the magnetization of CFO NPs did not saturate completely at 5 K compared to 300 K and 385 K. This is a typical signature of magnetism attributed, at

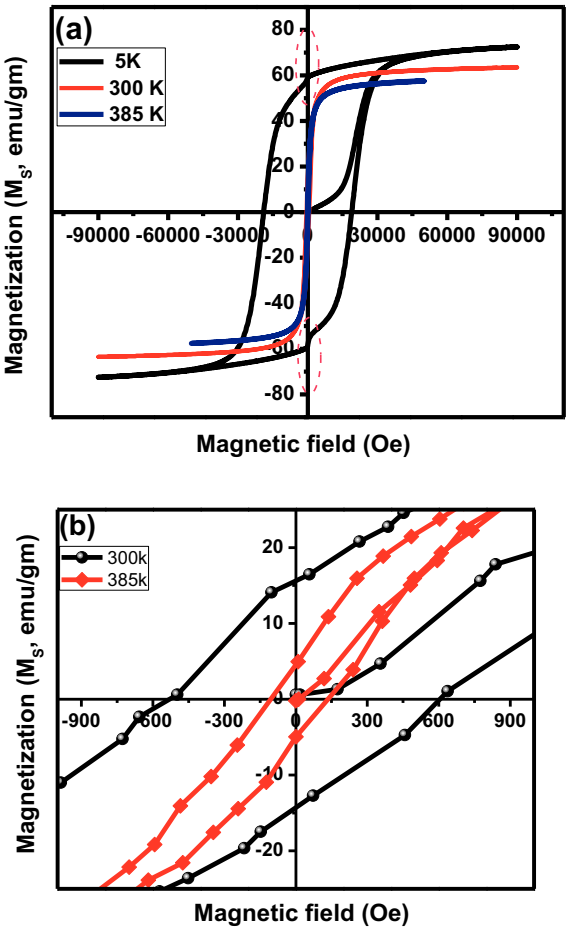


**Fig. 8.** M-H curve at three different temperatures 5 K, 300 K, and 385 K (a) and magnified M-H curve data at 300 K and 385 K for clarity (b) for pristine CFO NPs.

nanoscale, to spin canting at the NP surface [56]. This means that, at 5 K, the surface spins are not perfectly aligned with the core but tilted away from the anisotropy axis of the NPs. The value of coercivity ($H_C$) for CFO NPs at 5 K is 18.92 kOe, which is remarkably superior value compared to that of bulk CFO ($\sim$5 kOe at 5 K) [58]. It is an important to note that the exceptionally very high value of $H_C$ for CFO NPs synthesized using this approach has not been observed previously. Comparison of the $H_C$ values along with the corresponding particle size for the CFO NPs as documented in the literature is presented in Table 4. The chemistry and physics behind the remarkable $H_C$ value of these CFO NPs can be understood as follows. It is well known that $H_C$ is determined by the nature of anisotropy, which is very sensitive to factors such as the particle size, size-distribution, morphology, surface spin, and the interaction between NPs. However, in these CFO NPs, the effective anisotropy (originates from surface contribution) and interactions between NPs are the predominant factors that influence $H_C$. Therefore, to further understand the fundamental mechanism, the effective anisotropy constant ($K_E$) values are determined by fitting high magnetic field part of M-(H) data to the 'law of approach' (LA) to saturation. For a polycrystalline magnetic material, the 'law of approach' (LA) to saturation [47] states:

$$M(H) = M_S\left(1-\frac{a}{H}-\frac{b}{H^2}-\ldots\right) + \chi_p H \tag{9}$$

where M(H) is the magnetization at applied field (H), and $M_S$ is the saturation magnetization. The term $\chi_p$ is the forced magnetization coefficient that describes the linear increase in spontaneous magnetization at higher magnetic fields. This factor is applicable at high field

**Table 3**
Magnetic parameters obtained for pristine CFO NPs.

| Temperature (K) | Saturation magnetization ($M_S$) (emu/gm) | Saturation magnetization ($M_S$) ($\mu_B$/F.U) | Remanent magnetization ($M_r$) (emu/g) | Coercivity ($H_C$) (KOe) | Effective anisotropy × $10^6$ (erg/cm$^3$) $K_E = H_C \times M_S/0.64$ | Squarness ratio Mr/Ms |
|---|---|---|---|---|---|---|
| 5 | 72.785 | 3.183 | 58.705 | 18.92 | 11.54 | 0.81 |
| 300 | 63.533 | 2.669 | 15.119 | 0.569 | 0.303 | 0.24 |
| 385 | 57.625 | 2.421 | 4.797 | 0.120 | 0.580 | 0.08 |

| Parameters obtained from 'law of approach' (LA) to saturation | | | | Magnetic grain | | Maximum-dipolar field (Oe) | |
|---|---|---|---|---|---|---|---|
| Temperature (K) | Saturation magnetization $(M_S)_{fit}$(emu/gm) | $b$ (×$10^{10}$) (Oe$^2$) | Effective anisotropy ($K_E$) × $10^6$ (erg/cm$^3$) | Volume ($V_m$) (nm$^3$) | size($D_m$) (nm) | $(H_{dip})_{exp}$ | $(H_{dip})_{fitted}$ |
| 5 | 74.466 ± 0.012 | 0.0219 | 11.45 | 60.59 | 4.87 | 14.46 | 14.80 |
| 300 | 64.440 ± 0.006 | 0.1183 | 7.282 | 95.29 | 5.67 | 19.86 | 20.14 |
| 385 | 58.46 ± 0.008 | 0.0040 | 3.860 | 179.66 | 7.00 | 33.96 | 34.45 |

**Table 4**
The observed $H_C$ values (measured at 5 K) with the corresponding particle size compared to the literature.

| | | | | | | | |
|---|---|---|---|---|---|---|---|
| Coercivity (kOe) | 6.6 | 10.4 | 12.3 | 17.0 | 11.84 | 0.44 | 18.92 |
| Particle size (nm) | 7.3 | 38 | 16 | 12 | 23.5 | 14.9 | 12.29 |
| Ref. | [28] | [29] | [26] | [26] | [58] | [58] | This work |

and high temperature. This term is really small at temperatures below the Curie temperature ($T_c$) (for bulk CFO, $T_C \sim 798$ K), thus, it may be neglected. The term a/H is attributed to the strain field around dislocation in the material and it is also neglected in the present study. The term b/H$^2$ is the magnetic anisotropy and the coefficient $b$ is related to $K_E$ by:

$$b = \frac{4K_E^2}{15M_S^2} = \frac{4\left(K_{Sh}^2 + K_{St}^2 + K_{Sf}^2 + \frac{2}{7}K_1^2\right)}{15M_S^2} \quad (10)$$

where $K_{sh}$, $K_{st}$, $K_{sf}$ and $K_1$ are the shape anisotropy, stress anisotropy, surface anisotropy and magnetocrystalline anisotropy, respectively. The parameters, $b$ and $M_s$ as obtained through the fitting are used to determine $K_E$ at 5 K, 300 K and 385 K. Fig. 9 shows the linear fitted region of M-H curve in the range of 80–90 kOe at H = ± 90 kOe at 5 K and 300 K. The values of $K_E$ are summarized in Table 3. As stated earlier, compared to previous reports including our own, a large value of $H_C$ is noted at 5 K. Furthermore, for non-interacting, randomly oriented spherical particles with cubic anisotropy, $H_C = 0.64K_E/M_S$, where $K_E$ is the effective anisotropy constant. Using this relation, $K_E$ values are calculated for CFO NPs and tabulated in Table 3. It is noted that, only at 5 K, $K_E$ value agrees well with that obtained from 'law of approach' method as expected. From Table 3, it is seen that the CFO NPs (only at 5 K) exhibits the cubic anisotropy since it has squarness ratio 0.81 (at 5 K). Importantly, in the present work, $K_E$ values are larger (11.45 × $10^6$ erg/cm$^3$) than that of CFO NPs obtained by other methods (3.53 × $10^6$ erg/cm$^3$ at 5 K [28], 9.90 × $10^6$ erg/cm$^3$ at 10 K [30]) and that of bulk CFO (1.8–3.0 × $10^6$ erg/cm$^3$) at 300 K [27,28]. In addition, with decreasing temperature from 385 K to 5 K, the $K_E$ value increases; the highest value was noted as 11.45 × $10^6$ erg/cm$^3$ at 5 K. The very high $H_C$ and $K_E$ values are believed to be resulting from the surface anisotropy of canted spins at the NP surface [27].

Interestingly, jumps in the M-H curve at 5 K (Fig. 8a) curve are noted whenever the applied magnetic field become zero from both positive and negative saturated magnetization states. This can be attributed to the low temperature spin reorientation and the crystal alignment of CFO nanospheres. However, this behavior seems to be shape dependent since such jumps are observed in nanotubes [29] but are not observed in CFO nanorods [59] and nanowires [60]. Spin reorientation, at low temperatures, mostly originates from the reorientation of surface spins around particles [27]. Furthermore, such a kink is also attributed to the domain-wall pinning, which occurs when the direction of applied field changes to the opposite direction of spin. Presence of kink around the remanence, during the magnetization reversal process is attributed to the presence of magnetic exchange coupling between the hard and soft MNPs and inter-particle interactions

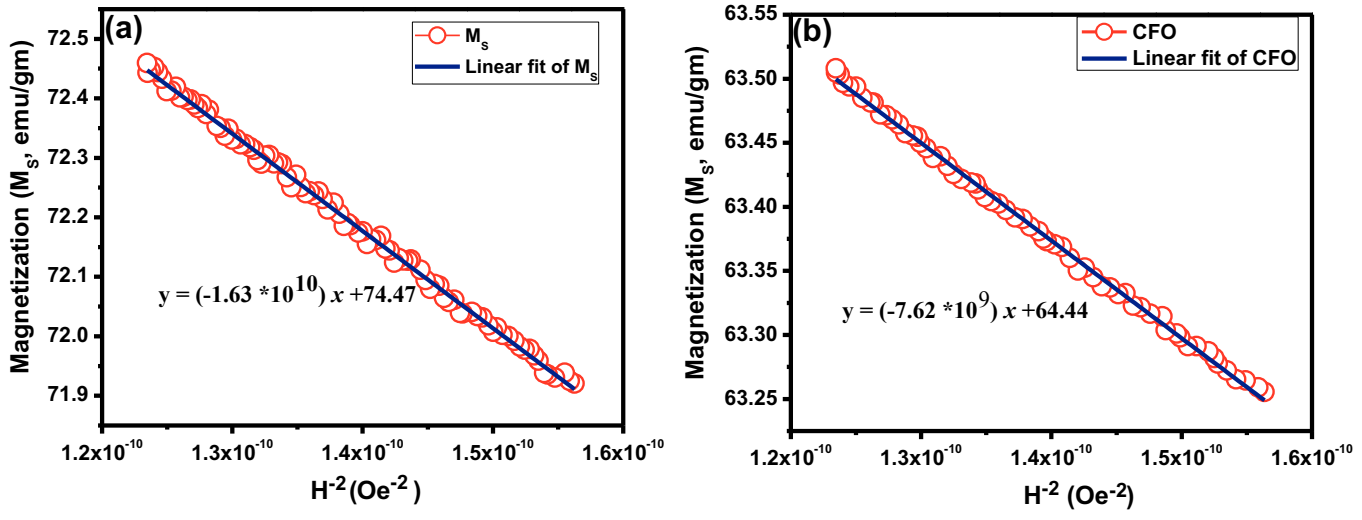


**Fig. 9.** Linear fitted region of M-H curve in the magnetic field from (80 kOe to 90 kOe) at 5 K (a) and 300 K (b) for CFO NPs.

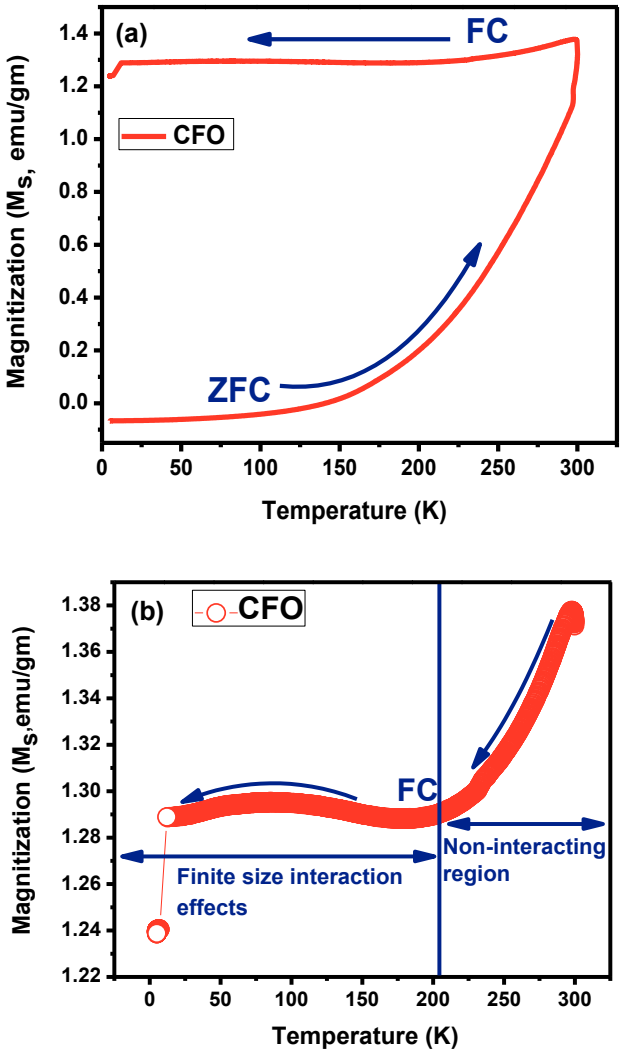


**Fig. 10.** ZFC and FC curves of CFO NPs measured at an applied magnetic field of 100 Oe (a) with the FC curve plotted separately and (b) for CFO NPs.

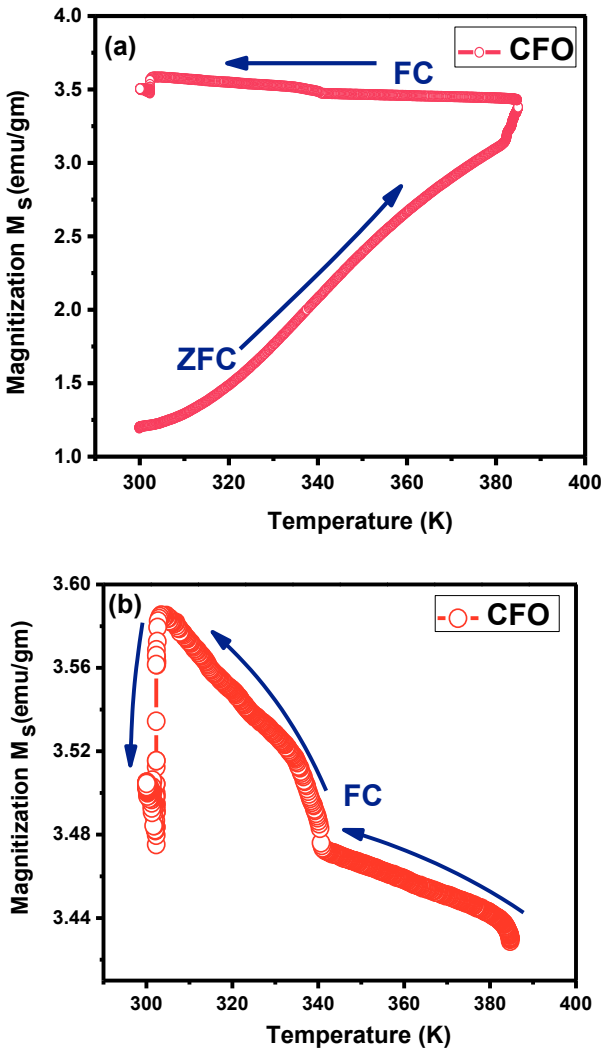


**Fig. 11.** ZFC and FC curves measured at an applied magnetic field of 100 Oe (a) along with FC curve plotted separately and (b) for CFO NPs.

[61]. In the present work, CFO is a single phase material without any impurities. Therefore, we neglect the possibility of exchange between the hard and soft MNPs and believe that the observed kink may be from spin reorientation of surface spin and interparticle interaction. Since the kinks were clearly observed but only at 5 K, spin reorientation of surface spin and the surface anisotropy contribution is dominating at 5 K compared to 300 K and 385 K. Moreover, the presence of interparticle interactions is also in agreement with the results obtained from FC and ZFC measurements (Figs. 10 and 11). In this case, the FC magnetization curve displays almost a constant value below certain temperatures (204 K, see Fig. 10(b)), lower than the blocking temperature $T_B$, and such a value is much higher than that of ZFC magnetization value. The ZFC data exhibits a decrease in magnetization ($M_{ZFC}$) with the decreasing temperature from 300 to 5 K due to the magnetic anisotropy-induced loss of long-range ferrimagnetic ordering in the nanocrystalline CFO. During FC, the magnetic moments aligned to minimize the Helmholtz free energy ($\Delta H \sim 0$). Hence, the bifurcation can be seen in the FC and ZFC curves. However, it requires a very large magnetic field to overcome the surface effect in nanocrystalline materials. Therefore, considerable bifurcation is not observed in the ZFC and FC curves (see Fig. 10(a)). The ZFC curve of NPs is usually characterized by a cusp at a particular temperature known as the blocking temperature, $T_B$. It is well known that above $T_B$, the materials are found in a superparamagnetic state with almost zero $H_C$, while a hysteresis loop appears below $T_B$. The ZFC curve (see Fig. 10) decreases monotonically down to a certain temperature (~212 K). Furthermore, it can be seen that the FC magnetization initially decreases monotonically with decreasing temperature in the range from 300 K to 205 K at 100 Oe which corresponds to non-interacting regions and then shows nearly saturated behaviour below 205 K, showing temperature independence (see Fig. 10b). This may be a consequence of finite-size interaction effects which occur from dipolar interactions and interparticle coupling interactions [2].

Further the ZFC-FC measurements were made in the temperature range of 300–385 K at an applied field of 100 Oe and the results are presented in Fig. 11(a). To better understand the magnetic behavior at nanoscale, the FC curve (300–385 K range) is shown in Fig. 10(b). It is noted that, in this 300–385 K range, $M_{FC}$ increases with decreasing temperature. Initially, the rate of $M_{FC}$ increase is small in the range from 385 to 340.59 K, whereas the rate of $M_{FC}$ increase is high from 340.59 to 304 K. After 304 K, it falls down and continues to decrease with lowering temperature and attains saturation. This type of increasing behavior of $M_{FC}$ with a decreasing temperature was observed in CFO nanotubes [29]. Thus, this behavior may be correlated to the larger magnetocrystalline anisotropy caused by geometrical shapes and inter-particle interactions of individual CFO NPs. TEM imaging analysis of CFO NPs with the cube and sphere shape morphology also provides evidence for the geometrical shape contribution to elevate the magnetocrystalline anisotropy. Furthermore, an inter-particle interaction of

individual CFO NPs also plays an important role. We believe that these two factors are responsible to $M_{FC}$ increase in the range of 300–385 K. Moreover, in this temperature range, the $M_{ZFC}$ value increases and attains the maximum ($T_{max}$) at 384.9 K. As explained by Peddis et al. [62], $T_{max}$ shift to higher temperatures can occur due to the increase of volume anisotropy and interparticle interaction. The $T_{max}$ and $T_B$ are related, in a first approximation, as: $T_{max} = AT_B$, where the constant A is between 1 and 2.73. Thus, in the present study, $T_B$ is estimated to be 384.9 K. Relatively larger $T_B$ might be due to the large anisotropy of CFO [2,55]. Thus, CFO NPs exhibit the superparamagnetic character above 385 K and, therefore, lower values of $H_C$ are noted at 385 K. Importantly, the presence of a frustrated surface spin layer, as suggested by the lack of saturation of the magnetization curve can strongly contribute to the decrease of remnant magnetization to ~4.80 emu/g at 385 K.

The magnetic grain volume, $V_m$, is calculated by using $T_B = K_E V_m / 25k_B$, where $K_E$ is the effective anisotropy constant and $k_B$ is the Boltzmann constant [27]. Subsequently, the magnetic grain diameters $D_m$ were also determined for CFO NPs at 5 K, 300 K and 385 K, respectively. All these parameters are listed in Table 3. It can be noted that the magnetic grain size $D_m$ (at 5 K, 300 K and 385 K) is smaller than the average physical size from various measurements, $D_{TEM} \equiv 10.53 \pm 0.28$ nm, $D_{FE\text{-}SEM} \equiv 14.84 \pm 0.20$ nm, and $D_{XRD} \equiv 12.29 \pm 0.15$ nm. This may be due to the presence of layer with canted surface spins around NPs. Using $D_{FE\text{-}SEM}$ and $D_m$, the volume ratio of the physical size ($D_{FE\text{-}SEM}$) (i.e. surface spin layer) to magnetic grain size ($D_m$) (i.e., the magnetically ordered core) is estimated are 28.23, 17.95, and 9.52 at5, 300 and 385 K, respectively. Similarly, the volume ratio values of the $D_{TEM}$ to $D_m$ (at 5, 300 and 385 K) are 10.11, 6.43, and 3.41, respectively. These values clearly indicate that the volume of the surface spin layer is larger than that of magnetically ordered core leading to a large surface anisotropy and, thus, large coercivity at 5 K. Generally, in case of MNPs or nanoclusters, the number of surface spins is comparable (or even larger than) to the number of core spins and, therefore, the surface anisotropy has a greater strength than the core anisotropy because of the local symmetry breaking.

The strength of interparticle dipolar interactions for CFO NPs is estimated by the maximum dipolar field ($H_{dip}$) between nearest neighbor particles using: $H_{dip} = 2\mu/d^3$, where $\mu$ is the particle moment ($\mu = M_S \times V_m$) and $d$ is the distance between the centers of two particles [47]. To determine $H_{dip}$ appropriately, we have considered the experimental $M_S$ value and fitted value of $M_S$ obtained from the 'LA' approach. The $(H_{dip})_{exp}$ and $(H_{dip})_{fit}$ values at 5 K, 300 K and 385 K, respectively, are also listed in Table 3. It is seen that the $H_{dip}$ at 385 K is double as compared to the value obtained at 5 K which may be due to the larger magnetic grain size. Moreover, it is evident (Table 3) that the squareness ratio ($R = M_r/M_S$) of CFO NPs at 5 K is much larger (R = 0.81) than those of reported values, 0.68 at 5 K [63], 0.75 at 5 K [28], and 0.6 at 10 K [66], and slightly smaller than that of 0.88 at 5 K [68] and 0.85 at 10 K [29]. Peddis et al. [62] have reported that the large squareness ratio of 0.88 can be assigned to the magnetic anisotropy variation from uniaxial to cubic symmetry. However, the Stoner-Wohlfarth model [64–66] suggests that for non-interacting single-domain particles with randomly oriented easy axes, R ~ 0.5 for uniaxial anisotropy, and 0.832 ($K_1 > 0$) or 0.87 ($K_1 < 0$) for cubic anisotropy [68]. CFO has cubic anisotropy with first magnetocrystalline anisotropy constant $K_1 > 0$; so, theoretical *R* should be 0.832. In the present work, for CFO NPs it is 0.81 (at 5 K), which is very close to the theoretical value of cubic anisotropy. Furthermore, the R value determines the presence or absence of different types of inter-grain group exchanges. It has been reported that for $R < 0.5$, the particle can interact by magnetostatic interaction while for $R = 0.5$, randomly oriented non interacting particles that undergo coherent rotations [2]. Finally, $0.5 < R < 1$ confirms the existence of exchange-coupling particles. Accordingly, the particle interaction in CFO NPs corresponds to the magnetostatic interaction and exchange coupling interactions are among the grains at 300 K, 385 K, and 5 K, respectively.

Moreover, the size of NPs, particle size distribution, surface functionalization, morphology and nature of agglomeration of NPs plays the crucial role to control the coercivity, effective anisotropy constant ($K_E$) and blocking temperature ($T_B$). As reported in our previous study [2], without using any surface coatings, CFO NPs of size 4.7 nm (from SAXS analysis) exhibit superparamagnetic behavior at 300 K with a blocking temperature ($T_B$) less than the room temperature but effective anisotropy constant ($K_E = 4.564 \times 10^6$ erg/cm$^3$ at 300 K) higher compared to bulk CFO ($1.8–3.0 \times 10^6$ erg/cm$^3$) but was found to be less than that of the present work ($K_E = 7.282 \times 10^6$ erg/cm$^3$ at 300 K). The blocking temperature of nanospinels is known to be influenced by the spin-orbit interaction in constituent metal ions ($Co^{2+}$, $Fe^{3+}$) [70]. For nanocrystallites with the same size, there can be a different occupation of the A (tetrahedral) and B (octahedral) sites by $Co^{2+}$ and $Fe^{3+}$, and cations in these two different site symmetries exhibit different spin-orbit couplings [67]. Several studies, mainly on CFO, have shown that $T_B$ also depends on the synthesis method [67]. Furthermore, the increase in $T_B$ was then linked to the increase of $Co^{2+}$ ions at the octahedral site [68,69]. On the other hand, size of NPs also affect the $T_B$. Besides particle size, the blocking temperature can also be influenced by several intrinsic factors, which are mainly magnetocrystalline, surface and shape anisotropy and extrinsic factors, which are related to the interactions between NPs. As discussed above, the surface anisotropy of canted spins at the particle surface mainly contribute or responsible for a large value of $K_E$. Moreover, the surface functionalization of CFO NPs with PEG is observed by IR spectrum. The hydrodynamic radius ($R_H$) obtained in different solvents is found to be larger compared to the size measured from FE-SEM, and SAS analyses which supports the fact that CFO NPs surface is functionalized with PEG. For spherical particles, $K_{eff}$ is expressed as:

$$K_{eff} = K_A + \left(\frac{6}{d}\right)K_S \tag{11}$$

where $K_A$ is the magnetocrystalline anisotropy, $d$ is the diameter of particle, and $K_S$ is the surface anisotropy. Surface anisotropy depends upon the surface properties and surface coating. In the present work, the surface of CFO is coated with PEG; therefore, surface anisotropy may be developed through chemical origin i.e., PEG molecules. Moreover, our results are consistent with the observations reported by other groups [24,69–71] who have noted that: (a) differential ligand-surface interactions may be responsible for altering the observed surface spin-canting disorder. (b) $T_B$, $M_r/M_S$ and $H_C$ values generally increases with increasing nanoparticle size. (c) At 5 K, both the $H_C$ and $M_r/M_S$ are increased compared to the values obtained at 300 K and 385 K. The strong effective anisotropy originated mainly from the surface spins, and may be responsible for the large Hc and Mr/Ms values of the CFO NPs. (d) Additionally, an inherent origin of the jumps observed around H = 0 was attributed to the low temperature reorientation of surface spins at low temperature, the crystal alignment of CFO nanospheres, domain-wall pinning, and interparticle interactions among the NPs (e) The magnetic grain size of the sample indicates that the canted surface spins exist around the magnetic particles (f) At 300 K and 385 K, the effective anisotropy of the sample obviously decreased because it arises mainly from the magnetocrystalline anisotropy and increased dipolar interaction with negligible contribution from surface spins (g) the size (diameters) obtained by TEM and XRD (SAXS) are consistent with each other.

### 3.7. In vitro cytotoxicity of CFO nanoparticles

Our objective is to investigate the cellular viability response to CFO NPs using the two types of cells, namely, A2780/CP70, (Cisplatin resistant ovarian cancer cell line) and human PBMC (normal peripheral blood mononuclear cells) via a modified MTT assay. A2780/CP70 cells

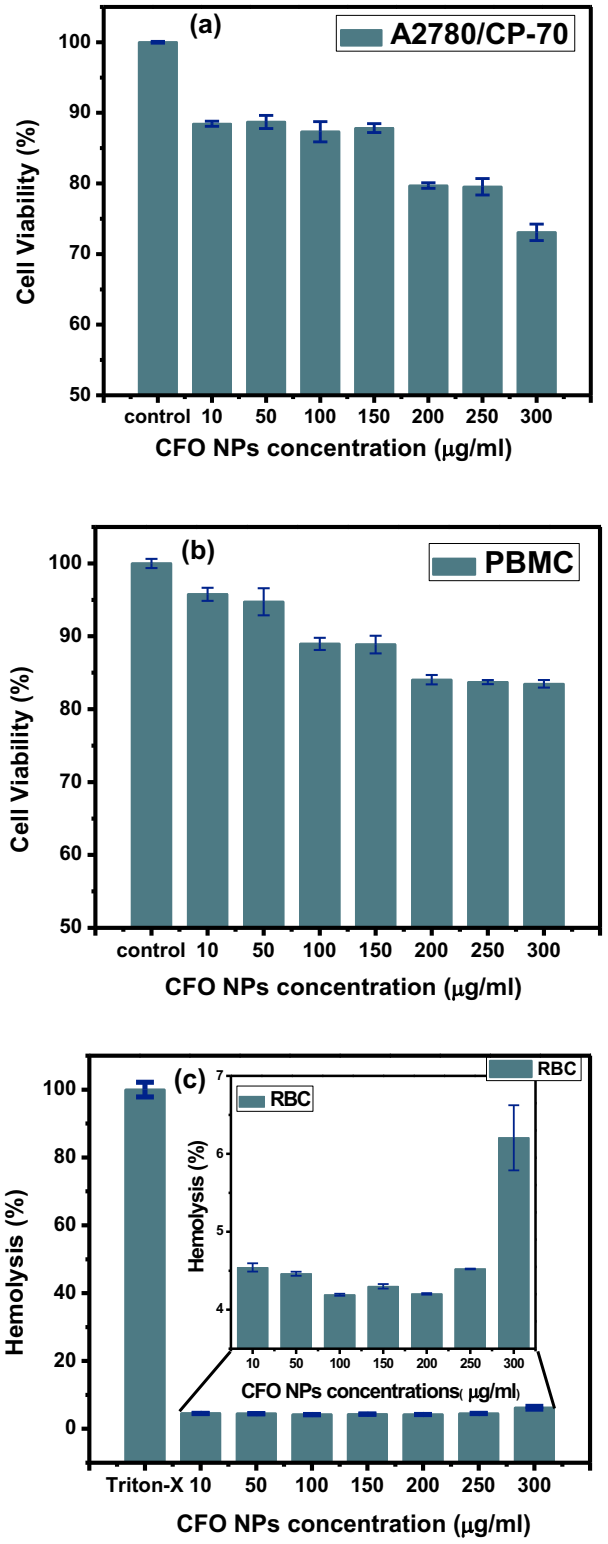


**Fig. 12.** Effect of different concentration of pristine CFO NPs on viability of (a) A2780/CP-70 cells, (b) human peripheral blood mononuclear cells (PBMC), after incubation for 24 h measured by modified MTT assay and (c) percentage of hemolysis of RBCs treated with CFO NPs (where Triton-X: Positive control).

were preferentially selected for the cytotoxicity analysis induced by CFO NPs to provide insights into the ovarian cancer the rapeutics investigations; because, it is found that ovarian cancer is the leading cause of death from gynecologic cancer in women worldwide. In addition, according to the National Cancer Institute, USA, the ovarian cancer has highest mortality rate among the reproductive cancers in women. The cytotoxicity data of pristine and sonicated CFO NPs against A2780/CP70 cells are shown in Fig. 12a. It is observed (Fig. 11(a)) that the cell viability is significantly reduced to 88.44%, 88.71%, 87.32%, 87.84%, 79.69%, 79.52% and 73.07% for the CFO concentrations of 10, 50, 100, 150, 200, 250 and 300 μg/ml, respectively. It indicates the proliferation of A2780/CP70 cells may get inhibited in a dose dependent manner over a wide concentration (10–300 μg/ml) of CFO NPs. This is supported by the previous results [2] in which the NPs showed cytotoxicity inhibition in dose dependent manner. Significantly, the observed cell viability of NPs is above 73% for all the different particle concentrations of CFO NPs. In conclusion, the cytotoxicity of A2780/CP70 seemed to be between 11.29 and 26.99% (viability ~ 73.01–88.71%) for 10 to 300 μg/ml concentration of 8.48 nm sized CFO NPs. In our previous study [2], CFO NPs of size 4.24 nm exhibits the cytotoxicity between 14 and 26 % (viability ~ 74–85%) for 10–300 μg/ml concentration of CFO NPs. Interestingly, the cytotoxicity of CFO NPs of 4.7 nm was compared with that of various corresponding concentrations of CFO NPs of 8.48 nm. Therefore, we can predict that the cytotoxicity of CFO NPs followed a dose- and size-dependent manner. These findings are similar to the reported work by others [72,73]. Moreover, the particle size was generally accepted as a fundamental factor in toxicity, with smaller particles tending to be more toxic. In this context, we have observed that the CFO NPs are quite more cytotoxic against the human cisplatin resistant ovarian cancer cells (A2780/CP70).

In continuation with the cytotoxicity studies on CFO NPs, we have also investigated the effect of CFO NPs on the proliferation of PBMC in vitro and shown in Fig. 11b. Interestingly, the PBMC exhibited higher cell viability (above 83%) over a wide range of concentration (10–300 μg/mL) of CFO NPs. Briefly, the cytotoxicity against PBMC was observed in the range 4.23–16.65% (viability: 83.48–95.77%) for 10 to 300 μg/ml concentration of CFO NPs. Moreover, cytotoxicity against the PBMC (4.23–16.652%) is observed to be lower compared to the cytotoxicity observed against the A2780/CP70 (11.29–26.99%). From a safety point of view, a careful analysis of cytotoxicity analysis of CFO NPs against cancer and normal cells suggested that the CFO NPs with concentrations up to 300 μg/ml can be used for biomedical applications. Moreover, it is quite evident from Fig. 12(b) that the CFO NPs did not show any adverse effects on PBMC compared to the control. Therefore, we suggest that these NPs can be tested as anticancer agents either alone or with existing drugs and it can also be used as a vector to deliver drugs to the affected area (body).

### 3.8. Hemolytic behavior of RBCs

It is well known that an excellent blood compatibility is desirable in vivo applications of the MNPs and also the MNPs having very low hemolytic effect (recommended range < 5%) are preferable for vivo applications. In the present work, hemolytic assays were performed to evaluate the blood compatibility of pristine CFO NPs at different concentrations (10–300 μg/ml). The quantities of RBCs haemolysis are compared with the controls. Fig. 12(c) depicts the release hemolytic profile in the control as well as in the presence of NPs. The absorbance values obtained at different concentrations of NPs showed no significant differences when compared to the control upto NPs concentration range of 250 μg/ml. In other words, upto 250 μg/ml concentrations of CFO NPs hemolytic effect is less than that of recommended range (< 5%). Thus, it can be concluded that the 8.48 nm sized CFO NPs have negligible hemolytic activity upto 250 μg/ml means, upto 250 μg/ml concentration, the CFO NPs having size 8.48 nm sized are compatible with human RBC. It is an essential feature required for in vivo biomedical applications such as drugs, in drug delivery, intravenous drug delivery applications without creating any harmful effects in the blood stream.

## 4. Conclusions

$CoFe_2O_4$ NPs were synthesized using facile, modified hydrothermal chemical route at low temperature (180 °C). The modified hydrothermal approach is efficient in terms of high yield (~84%) synthesis of CFO NPs with a controlled morphology (from spherical to cubic shape) and remarkably high coercivity (18.92 kOe) compared to other existing reports in the literature. The CFO NPs are highly crystalline, exhibits narrow size distribution and stable in aqueous medium and DMEM. The XRD data along with Raman and Infrared spectroscopic studies indicate the formation of high quality cubic symmetry CFO NPs. The median size of basic CFO particles is 8.48 nm. CFO NPs demonstrate the superparamagnetic character at $T_B$ ~ 384.9 K. Low coercivity obtained at 300 K and 385 K implies the potential application in the high-density perpendicular recording media. The strong effective anisotropy mainly originated from the surface spins, and it may be responsible for the large $H_C$ and $Mr/M_S$ values of the CFO NPs. The magnetic grain size of the samples indicates that the canted surface spins exist around the magnetic particles. It is evident that this study has shown the underlying mechanism of superior Hc and bioapplicability of nanoscale cobalt ferrite systems in addition to help for improve magnetic performance of CFO NPs. In vitro cytocompatibility experiments revealed that nanoparticles were mildly anti-proliferative against human Cisplatin resistant ovarian cancer cell (A2780/CP70), and safe towards the normal cells. Negligible hemolytic activity implies that nanoparticles are compatible with human RBC, which is an essential feature for future in vivo biomedical applications such as drugs, in drug delivery, intravenous drug delivery applications without creating any harmful effects in the blood stream. Thus, the synthesized CFO NPs fulfill the emerging need for cheaper drugs or drug delivery vehicles with negligible side effects to the patients. Further, being non-hazardous to the environment also make them a suitable candidate for biomedical applications.

## Supplemental material

Additional details of the cytotoxic studies and procedures are presented. In addition, the TEM data statistical analysis and results are included.

## Acknowledgments

S. M. Ansari is thankful to BARC, India for providing the financial assistance (GOI-E-175) to carry out the research work. S. M. would like to thank Miss. Renuka D. Bhor of Department of Zoology, Savitribai Phule Pune University for her help in biological assay. B. B. Sinha thank the Department of Science and Technology (DST) (Government of India) for INSPIRE Young Scientist Award. Y. D. Kolekar thank the DST, India (Grant No.: 633 SR/FTP/PS-040/2010) for the financial assistance. Also, we are thankful to Dr. R. S. Devan, Metallurgy Engineering and Materials Science, Indian Institute of Technology (IIT), Indore for helping to avail the FE-SEM images. We acknowledge Dr. A. Abhyankar, Defence Institute of Advanced Technology (DIAT), Pune, India for help with the TEM images. The authors also acknowledge SAIF Mumbai for TEM analysis. C.V. Ramana acknowledges with pleasure the support from the National Science Foundation (NSF), USA, with NSF-PREM grant #DMR-1205302.

## References

[1] G.C. Lavorato, D. Peddis, E. Lima, H.E. Troiani, E.D. Agostinelli, R.D. Fiorani Zysler, E.L. Winkler, Magnetic interactions and energy barrier enhancement in core/shell bimagnetic nanoparticles, J. Phys. Chem. C 119 (2015) 15755–15762.

[2] S.M. Ansari, R.D. Bhor, K.R. Pai, S. Mazumder, D. Sen, Y.D. Kolekar, C.V. Ramana, Size and chemistry controlled cobalt-ferrite nanoparticles and their anti-proliferative effect against the MCF-7 breast cancer cells, ACS Biomater. Sci. Eng. 2 (2016) 2139–2152.

[3] R. Hudson, V. Chazelle, M. Bateman, R.C. Roy, J. Li, A. Moores, Sustainable synthesis of magnetic ruthenium-coated iron nanoparticles and application in the catalytic transfer hydrogenation of ketones, ACS Sust. Chem. Eng. 3 (2015) 814–820.

[4] S. Genc, B. Derin, Synthesis and rheology of ferrofluids: a review, Curr. Opin. Chem. Eng. 3 (2014) 118–124.

[5] Z. Skeete, H. Cheng, E. Crew, L. Lin, W. Zhao, P. Joseph, S. Shan, H. Cronk, J. Luo, Y. Li, Q. Zhang, C.J. Zhong, Design of functional nanoparticles and assemblies for theranostic applications, ACS Appl. Mater. Interfaces 6 (24) (2014) 21752–21768.

[6] J. Huang, L. Wang, R. Lin, A.Y. Wang, L. Yang, M. Kuang, M. Qian, H. Mao, Casein-coated iron oxide nanoparticles for high MRI contrast enhancement and efficient cell targeting, ACS Appl. Mater. Interfaces 5 (2013) 4632–4639.

[7] Violetta Georgiadou, George Makris, Dionysia Papagiannopoulou, Georgios Vourlias, Catherine Dendrinou-Samara, Octadecylamine mediated versatile coating of $CoFe_2O_4$NPs for the sustained release of anti-inflammatory drug naproxen and in vivo target selectivity, ACS Appl. Mater. Interfaces 8 (2016) 9345–9360.

[8] V.A.M. Brabers, Handbook of Magnetic Materials, vol. 8, North–Holland, Amsterdam, 1995, p. 212.

[9] S. Jovanović, M. Spreitzer, M. Tramšek, Z. Trontel, D. Suvorov, Effect of oleic acid concentration on the physicochemical properties of cobalt ferrite nanoparticles, J. Phys. Chem. C 118 (2014) 13844–13856.

[10] L. Tiano, G.C. Papaefthymiou, C.S. Lewis, J. Han, C. Zhang, Q. Li, C. Shi, A.M.M. Abeykoon, S.J.L. Billinge, E. Stach, J. Thomas, K. Guerrero, P. Munayco, J. Munayco, R.B. Scorzelli, P. Burnham, A.J. Viescas, S.S. Wong, Correlating size and composition-dependent effects with magnetic, Mössbauer, and pair distribution function, measurements in a family of catalytically active ferrite nanoparticles, Chem. Mater. 27 (2015) 3572–3592.

[11] B. Cai, M. Zhao, Y. Ma, Z. Ye, J. Huang, Bioinspired formation of 3D hierarchical $CoFe_2O_4$ porous microspheres for magnetic-controlled drug Release, ACS Appl. Mater. Interfaces 7 (2015) 1327–1333.

[12] S.F. Medeiros, A.M. Santos, H. Fessi, A. Elaissari, Stimuli-responsive magnetic particles for biomedical applications, Int. J. Pharm. 403 (2011) 139–161.

[13] X. Wu, Y. Tan, H. Mao, M. Zhang, Toxic effects of iron oxide nanoparticles on human umbilical vein endothelial cells, Int. J. Nanomed. 5 (2010) 385–399.

[14] K. Soto, K.M. Garza, L.E. Murr, Cytotoxic effects of aggregated nanomaterials, Acta Biomater. 3 (2007) 351–358.

[15] T.J. Brunner, P. Wick, P. Manser, P. Spohn, R.N. Grass, L.K. Limbach, A. Bruinink, W.J. Stark, In vitro cytotoxicity of oxide nanoparticles: comparison to asbestos, silica, and the effect of particle solubility, Environ Sci. Technol. 40 (2006) 4374–4381.

[16] T.R. Pisanic, J.D. Blackwell, V.I. Shubayev, R.R. Finones, S. Jin, Nanotoxicity of iron oxide nanoparticle internalization in growing neurons, Biomaterials 28 (2007) 2572–2581.

[17] A.L. Ortega, E. Lottini, C.J. Fernandez, C. Sangregorio, Exploring the magnetic properties of cobalt-ferrite nanoparticles for the development of a rare-earth-free permanent magnet, Chem. Mater. 27 (2015) 4048–4056.

[18] M. Houshiar, F. Zebhi, Z.J. Razi, A. Alidoust, Z. Askari, Synthesis of cobalt ferrite ($CoFe_2O_4$) nanoparticles using combustion, coprecipitation, and precipitation methods: a comparison study of size, structural, and magnetic properties, J. Magn. Magn. Mater. 371 (2014) 43–48.

[19] P. Jing, L. Pan, J. Du, J. Wang, Q. Liu, $SiO_2$-modified $CoFe_2O_4$ hollow nanofibers with flexible room temperature magnetic performance, Phys. Chem. Chem. Phys. 17 (2015) 12841–12848.

[20] G. Muscas, G. Singh, W.R. Glomm, R. Mathieu, P.A. Kumar, G. Concas, E. Agostinelli, D. Peddis, Tuning the size and shape of oxide nanoparticles by controlling oxygen content in the reaction environment: morphological analysis by aspect maps, Chem. Mater. 27 (2015) 1982–1990.

[21] G. Singh, P.A. Kumar, C. Lundgren, A.T.J. Helvoort, R. Mathieu, E. Wahlström, W.R. Glomm, Tunability in crystallinity and magnetic properties of core-shell Fe nanoparticles, Part. Part. Syst. Charact. 31 (2014) 1054–1059.

[22] (a) D. Selli, C.D. Valantin, Ab initio investigation of polyethylene glycol coating of $TiO_2$ surfaces, J. Phys. Chem. C 120 (2016) 29190–29201;
(b) B. Pelaz, P.D. Pino, P. Maffre, R. Hartmann, M. Gallego, S.R. Fernandez, J.M. Fuente, G.U. Nienhaus, W.J. Parak, Surface functionalization of nanoparticles with polyethylene glycol: effects on protein adsorption and cellular uptake, ACS Nano 9 (2015) 6996–7008.

[23] X. Wu, W. Wang, F. Li, S. Khaimanov, N. Tsidaeva, M. Lahoubi, PEG-assisted hydrothermal synthesis of $CoFe_2O_4$ nanoparticles with enhanced selective adsorption properties for different dyes, Appl. Sur. Sci. 389 (2016) 1003–1011.

[24] J. Frenkel, J. Doefman, Spontaneous and induced magnetisation in ferromagnetic bodies, Nature 126 (1930) 274–275.

[25] J.L. Dormann, D. Fiorani, E. Tronc, Advanced In Chemical Physics vol. XCVIII, Wiley & Sons, New York, 1997.

[26] V.B. Gutierrez, M.R. Virumbrales, S. Puche, J. Maria, Superparamagnetic behavior of $MFe_2O_4$ nanoparticles and $MFe_2O_4/SiO_2$ composites (M: Co, Ni), J. Phys. Chem. C 117 (2013) 20927–20935.

[27] S.T. Xu, Y.Q. Ma, G.H. Zheng, Z.X. Dai, Simultaneous effects of surface spins: rarely large coercivity, high remanence magnetization and jumps in the hysteresis loops observed in $CoFe_2O_4$ nanoparticles, Nanoscale 7 (2015) 6520–6526.

[28] S. Laureti, G. Varvaro, A.M. Testa, D. Fiorani, E. Agostinelli, G. Piccaluga, A. Musinu, A. Ardu, D. Peddis, Magnetic interactions in silica coated nanoporous assemblies of $CoFe_2O_4$ nanoparticles with cubic magnetic anisotropy, Nanotechnology 21 (2010) 315701.

[29] J.C. Fu, J.L. Zhang, Y. Peng, J.G. Zhao, G.G. Tan, N.J. Mellors, E.Q. Xie, W.H. Han, Unique magnetic properties and magnetization reversal process of $CoFe_2O_4$

nanotubes fabricated by electrospinning, Nanoscale 4 (2014) 3932–3936.
[30] R.N. Bhowmik, V. Vasanthi, A. Poddar, Alloying of $Fe_3O_4$ and $Co_3O_4$ to develop $Co_{3x}Fe_{3(1-x)}O_4$ ferrite with high magnetic squareness, tunable ferromagnetic parameters, and exchange bias, J. Alloys Compd. 578 (2013) 585–594.
[31] L. Wu, P.O. Jubert, D. Berman, W. Imaino, A. Nelson, H. Zhu, S. Zhang, S. Sun, Monolayer assembly of ferrimagnetic $Co_xFe_{3-x}O_4$ nanocubes for magnetic recording, Nano Lett. 14 (2014) 3395–3399.
[32] M.P. Morales, S.V. Verdaguer, M.I. Montero, C.J. Serna, A. Roig, L. Casas, B. Martinez, F. Sandiumenge, Surface and internal spin canting in $\gamma$-$Fe_2O_3$ nanoparticles, Chem. Mater. 11 (1999) 3058–3064.
[33] S. Mazumder, D. Sen, T. Saravanan, P.R. Vijayaraghavan, Performance and calibration of the newly installed medium resolution double crystal based small-angle neutron scattering instrument at trombay, J. Neutron. Res. 9 (2001) 39–57;
S. Mazumder, D. Sen, T. Saravanan, P.R. Vijayaraghavan, A medium resolution double crystal based small-angle neutron scattering instrument at Trombay, Curr. Sci. 81 (2001) 257–262.
[34] J.A. Lake, An iterative method of slit-correcting small angle, Acta Cryst. 23 (1967) 191.
[35] L. Kumar, P. Kumar, A. Narayan, M. Kar, Rietveld analysis of XRD patterns of different sizes of nanocrystalline cobalt ferrite, Int. Nano Lett. 3 (2013) 8.
[36] B.D. Cullity, Elements of X-ray Diffraction, Addison-Wesley, London, UK, 1978.
[37] V. Georgiadou, C. Kokotidou, B.L. Droumaguet, B. Carbonnier, T.C. Papadopoulou, C.D. Samara, Oleylamine as a beneficial agent for the synthesis of $CoFe_2O_4$ nanoparticles with potential biomedical uses, Dalton Trans. 43 (2014) 6377–6388.
[38] S.Y. Vilar, M.S. Andujar, C.G. Aguirre, A simple solvothermal synthesis of $MFe_2O_4$ (M = Mn, Co and Ni) nanoparticles, J. Solid State Chem. 182 (2009) 2685–2690.
[39] J. Dobryszycki, S. Biallozor, On some organic inhibitors of zinc corrosion in alkaline media, Corros. Sci. 43 (2001) 1309–1319.
[40] D.E. Zhang, X.J. Zhang, X.M. Ni, H.G. Zheng, D.D. Yang, Synthesis and characterization of $NiFe_2O_4$ magnetic nanorods via a peg-assisted route, J. Mag. Magn. Mater. 292 (2005) 79–82.
[41] O. Glatter, O. Kratky, Small Angle X-ray Scattering, Academic Press, New York, NY, 1982.
[42] J. Texeira, Small-angle scattering by fractal system, J. Appl. Crystallogr. 21 (1988) 781–785;
D. Sen, J. Bahadur, S. Mazumder, T. Mahata, M. Syambabu, P.K. Sinha, Investigation on pore structure and small-scale agglomeration behaviour in liquid phase sintered SiC using small angle neutron scattering, Pramana. J. Phys. 71 (5) (2008) 979–984.
[43] J.S. Pedersen, Determination of size distribution from small angle scattering data for systems with effective hard sphere interactions, J. Appl. Crystallogr. 27 (1994) 595–608;
A. Das, D. Sen, S. Mazumder, A.K. Ghosh, C.B. Basak, K. Dasgupta, Formation of nano-structured core–shell microgranules by evaporation induced assembly, RSC Adv. 5 (2015) 85052–85060.
[44] A. Guinier, G. Fournet, B.C. Walker, L.K. Yudowith, Small Angle Scattering of X-Rays, Wiley, New York, 1955.
[45] A. Thangaraja, V. Savitha, K. Jegatheesan, Preparation and characterization of polyethylene glycol coated silica nanoparticles for drug delivery application, Int. J. Nanotechnol. Appl. 1 (2010) 31–38;
M.R. Phadatare, V.M. Khot, A.B. Salunkhe, N.D. Thorat, S.H. Pawar, Studies on polyethylene glycol coating on $NiFe_2O_4$ nanoparticles for biomedical applications, J. Magn. Magn. Mater. 324 (2012) 770–772.
[46] I. Sharifi, H. Shokrollahi, M.M. Doroodmand, R. Safi, Magnetic and structural studies on $CoFe_2O_4$ nanoparticles synthesized by co-precipitation, normal micelles and reverse micelles methods, J. Magn. Magn. Mater. 324 (2012) 1854–1861.
[47] S.M. Ansari, R.D. Bhor, K.R. Pai, D. Sen, S. Mazumder, K. Ghosh, Y.D. Kolekar, C.V. Ramana, Cobalt nanoparticles for biomedical applications: facile synthesis, physiochemical characterization, cytotoxicity behavior and biocompatibility, Appl Surf. Sci. 414 (2017) 171–187.
[48] V.B. Bregar, J. Lojk, V. Šuštar, P. Veranič, M. Pavlin, Visualization of internalization of functionalized cobalt ferrite nanoparticles and their intracellular fate, Int. J. Nanomed. 8 (2013) 919–931.
[49] K. Maaz, A. Mumtaz, S.K. Hasanian, A. Celyan, Synthesis and magnetic properties of cobalt ferrite ($CoFe_2O_4$) nanoparticles prepared by wet chemical route, J. Magn. Magn. Mater. 308 (2007) 289–295.
[50] R.A. Bohara, N.D. Thorat, H.M. Yadav, S.H. Pawar, One-step synthesis of uniform and biocompatible amine functionalized cobalt ferrite nanoparticles: a potential carrier for biomedical applications, New J. Chem. 38 (2014) 2979–2986.
[51] K. Sinko, E. Manek, A. Meiszterics, K. Havancsák, U. Vainio, H. Peterlik, Liquid-phase syntheses of cobalt ferrite nanoparticles, J. Nanopart. Res. 14 (2012) 894.
[52] D.J. Tobler, S. Shaw, L.G. Benning, Quantification of initial steps of nucleation and growth of silica nanoparticles: an in situ SAXS and DLS study, Geochim. Cosmochim. Acta 73 (2009) 5377–5393.
[53] Y.F. Shen, J. Tang, Z.H. Nie, Y.D. Wang, Y. Ren, L. Zuo, Tailoring size and structural distortion of $Fe_3O_4$ nanoparticles for the purification of contaminated water, Bioresource Technol. 100 (2009) 4139–4146.
[54] C.R. Lin, Y.M. Chu, S.C. Wang, Magnetic properties of magnetite nanoparticles prepared by mechanochemical reaction, Mater. Lett. 60 (2006) 447–450.
[55] S. Sun, H. Zeng, D.B. Robinson, S. Raoux, P.M. Rice, S.X. Wang, G. Li, Monodisperse $MFe_2O_4$ (M = Fe Co, Mn) nanoparticles, J. Am. Chem. Soc. 126 (1) (2003) 273–279.
[56] T. Bala, C.R. Sankar, M. Baidakova, V. Osipov, T. Enoki, P.A. Joy, B.L.V. Prasad, M. Sastry, Cobalt and magnesium ferrite nanoparticles: preparation using liquid foams as templates and their magnetic characteristics, Langmuir. 21 (23) (2005) 10638–10643.
[57] G.C. Papaefthymiou, Nanoparticle magnetism, Nano Today 4 (5) (2009) 438–447.
[58] S. Bhattacharyya, J.P. Salvetat, R. Fleurier, A. Husmann, T. Cacciaguerra, M.L. Saboungi, One step synthesis of highly crystalline and high coercive cobalt-ferrite nanocrystals, Chem. Commun. 4818–4820 (2005).
[59] Z.T. Zhang, A.J. Rondinone, J.X. Ma, J. Shen, S. Dai, Morphologically templated growth of aligned spinel $CoFe_2O_4$ nanorods, Adv. Mater. 17 (2005) 1415–1419.
[60] Z. Wang, X. Liu, M. Lv, P. Chai, Y. Liu, X. Zhou, J. Meng, Preparation of one-dimensional $CoFe_2O_4$ nanostructures and their magnetic properties, J. Phys. Chem. C 112 (2008) 15171–15175.
[61] M.F. Hansen, S. Mørup, Estimation of blocking temperatures from ZFC/FC Curves, J. Magn. Magn. Mater. 203 (1999) 214–216.
[62] D. Peddis, F. Orrù, A. Ardu, C. Cannas, A. Musinu, G. Piccaluga, Interparticle interactions and magnetic anisotropy in cobalt ferrite nanoparticles: influence of molecular coating, Chem. Mater. 24 (2012) 1062–1071.
[63] G.C.P. Leite, E.F. Chagas, R. Pereira, R.J. Prado, A.J. Terezo, M. Alzamora, E.B. Saitovitch, Longitude magneto optical kerr effect of Fe/GaAs (001) with Al over layers, J. Magn. Magn. Mater. 324 (2012) 2711–2716.
[64] L. Kumar, P. Kumar, S.K. Srivastava, M. Kar, Low temperature and high magnetic field dependence and magnetic properties of nanocrystalline cobalt ferrite, J. Supercond. Nov. Magn. 27 (2014) 1677–1681.
[65] E.C. Stoner, E.P. Wohlfarth, A mechanism of magnetic hysteresis in heterogeneous alloys, Philos. Trans. Proc. R. Soc. Lond., Ser. A. Math. Phys. Sci. 240 (826) (1948) 599–642.
[66] J.M. Vargas, W.C. Nunes, L.M. Socolovsky, M. Knobel, D. Zanchet, Effect of Dipolar interaction observed in iron-based nanoparticles, Phys. Rev. B: Condens. Matter 72 (2005) 184428(1)–184428(6).
[67] E.F. Kneller, F.E. Luborsky, Particle size dependence of coercivity and remanence of single-domain particles, J. Appl. Phys. 34 (1963) 656–658.
[68] C. Liu, B. Zou, A.J. Rondinone, Z.J. Zhang, Chemical control of superparamagnetic properties of magnesium and cobalt spinel ferrite nanoparticles through atomic level magnetic couplings, J. Am. Chem. Soc. 122 (2000) 6263–6267.
[69] L. Ajroudi, N. Mliki, L. Bessäs, V. Madigou, S. Villain, C. Leroux, Magnetic, electric and thermal properties of cobalt ferrite nanoparticles, Mater. Res. Bull. 59 (2014) 49.
[70] C. Liu, Z.J. Zhang, Size-dependent superparamagnetic properties of mn spinel ferrite nanoparticles synthesized from reverse micelles, Chem. Mater. 13 (2001) 2092–2096.
[71] N. Moumen, M.P. Pileni, New syntheses of cobalt ferrite particles in the range of 2–5 nm: comparison of the magnetic properties of the nanosized paticles in dispersed fluid or in powder form, Chem. Mater. 8 (1996) 1128–1134.
[72] I. Papageorgiou, C. Brown, R. Schins, S. Singh, R. Newson, S. Davis, J. Fisher, E.C. Ingham, P. Case, The effect of nano- and micron-sized particles of cobalt-chromium alloy on human fibroblasts in vitro, Biomaterials 28 (2007) 2946–2958.
[73] Z.L. Shi, X. Huang, Y.R. Cai, R.K. Tang, D.S. Yang, Size effect of hydroxyapatite nanoparticles on proliferation and apoptosis of osteoblast-like cells, Acta Biomater. 5 (1) (2009) 338–345.